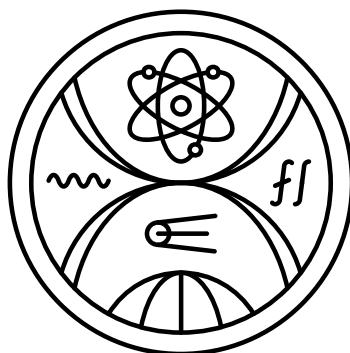


FACULTY OF MATHEMATICS, PHYSICS AND INFORMATICS
COMENIUS UNIVERSITY, BRATISLAVA



DECAY SPECTROSCOPY OF ^{186}Bi AND
PRODUCTION OF RADON AND RADIUM ISOTOPES
DISSERTATION THESIS

COMENIUS UNIVERSITY, BRATISLAVA
FACULTY OF MATHEMATICS, PHYSICS AND INFORMATICS

DECAY SPECTROSCOPY OF ^{186}Bi AND
PRODUCTION OF RADON AND RADIUM ISOTOPES
DISSERTATION THESIS

Study program: Nuclear and subnuclear physics
Department: Department of Nuclear Physics and Biophysics
Supervisor: doc. Mgr. Stanislav Antalic, PhD.
Consultant: Mgr. Boris Andel, PhD.

Bratislava, 2024

Mgr. Adam Sitarčík

Declaration of authorship

I hereby declare, that I personally carried out this dissertation project with help of my supervisor, consultant and with use of the listed literature and sources.

.....

Adam Sitarčík

Bratislava, 2024

Acknowledgments

I would like to thank my supervisor, doc. Mgr. Stanislav Antalic, PhD. for his priceless advice, comments, support and a lot of patience. Also, I would like to thank my colleagues for many interesting discussions, help and great working environment.

Abstract:

The fusion-evaporation reactions are a great tool for the production of neutron-deficient nuclei from the lead region. The structure of nuclei from this region manifests itself via a multitude of interesting phenomena, for example nuclear isomerism, intruder states, shape coexistence and many more. In this project, the structure of ^{182}Tl populated after an α decay of ^{186}Bi (produced in the $^{95}\text{Mo}(^{93}\text{Nb}, 2n)^{186}\text{Bi}$ and $^{46}\text{Ti}(^{144}\text{Sm}, p3n)^{186}\text{Bi}$ reactions) was investigated and preliminary results are presented. Several new levels could be identified on the basis of prompt $\alpha - \gamma$ coincidences. An alternative approach considering $\alpha + e^-$ summing effects is explained and employed, by the use of which four new transitions could be tentatively assigned to the ^{182}Tl .

The second part of the project is aimed to investigate the production of radon and radium neutron-deficient isotopes. The main goal is to determine the fission barrier scaling parameter for each reaction, by comparing theoretical cross sections obtained with the code HIVAP with the experimental ones. The theoretical background explaining the mechanisms of the fusion-evaporation reactions and all relevant decay modes is presented.

Key words: alpha decay, decay spectroscopy, fusion-evaporation reactions, cross section

Abstrakt:

Fúžno-výparné reakcie predstavujú výborný nástroj pre produkciu neutrónovo-deficitných jadier z oblasti olova. Štruktúra jadier z tejto oblasti sa prejavuje rôznymi zaujímavými javmi, ako napríklad jadrovou izomériou, tzv. "intruder" stavmi, tvarovou koexistenciou a mnohými ďalšími. V rámci projektu bolo študované jadro ^{182}Tl produkované po α rozpade ^{186}Bi (produkovaného v reakciách $^{95}\text{Mo}(^{93}\text{Nb}, 2n)^{186}\text{Bi}$ a $^{46}\text{Ti}(^{144}\text{Sm}, p3n)^{186}\text{Bi}$) a predbežné výsledky sú prezentované. Niekoľko nových stavov bolo identifikovaných na základe promptných $\alpha - \gamma$ koincidencií. Alternatívny prístup zohľadňujúci $\alpha - e^-$ sumácie je vysvetlený a použitý, vďaka nemu boli predbežne priradené ďalšie štyri prechody v ^{182}Tl .

Druhá časť projektu je zameraná na štúdium produkcie neutrónovo-deficitných izotopov radónu a rádia. Hlavným cieľom je určenie škálovacieho faktoru štiepnej bariéry pre každú študovanú reakciu, porovnaním teoretických účinných prierezov podľa kódu HIVAP s experimentálnymi hodnotami. Prezentovaný je teoretický základ popisujúci mechanizmus fúžno-výparných reakcií spolu s popisom relevantným rozpadových módov.

Kľúčové slová: alfa premena, rozpadová spektroskopia, fúžno-výparné reakcie, účinný prierez, štatistický kód

List of Abbreviations and Symbols

Z Atomic number (number of protons)

CE Conversion electron

CERN Conseil européen pour la recherche nucléaire - European organization for nuclear research

CN Compound nucleus

ER Evaporation residue

FER Fusion-evaporation reaction

FF Fission fragment

FWHM Full width at half maximum

g.s. Ground state

GSI Gesellschaft für Schwerionenforschung - Center for heavy ion research

HF Hindrance factor

IC Internal conversion

ICC Internal conversion coefficient

PSSD Position-sensitive silicon detector

SCC Scale Coulomb counter

SHIP Separator for heavy ion reaction products

TAC Time-to-amplitude converter

TOF Time of flight

UNILAC Universal linear accelerator

Contents

Introduction	1
1 Physical background	4
1.1 Fusion-evaporation reactions	4
1.1.1 Cross section of the fusion-evaporation reaction	7
1.2 Other types of reactions	11
1.3 Nuclear decays	11
1.3.1 Alpha decay	11
1.3.2 Internal transitions	15
1.4 Nuclear isomerism	19
1.4.1 Types of nuclear isomers	20
1.5 Methods for nuclear structure studies	20
1.5.1 Decay spectroscopy	20
1.5.2 Laser spectroscopy	20
1.5.3 In-beam spectroscopy?	20
2 Experimental Background	21
2.1 Experimental production of nuclei	21
2.2 Nuclei separation - SHIP	22
2.3 Detector system	24
2.4 Data analysis	27
2.4.1 Electronics and signal processing	27
2.4.2 Time-position correlation technique	28
2.4.3 Statistical analysis in case of poor statistics	30
3 Objectives of the project	33
3.1 Decay spectroscopy of ^{186}Bi	33
3.1.1 Previous studies of ^{186}Bi	34
3.2 Cross section studies	35
3.2.1 Previous studies of the cross section systematics in the lead region	35

4	Preliminary results	37
4.1	Investigation of ^{186}Bi	37
4.1.1	Experimental details	37
4.1.2	Alpha–gamma coincidence approach	37
4.1.3	Alpha(+CE)–gamma approach	42
5	Summary	44

Introduction

Even after more than 100 years since the discovery of the atomic nucleus by E. Rutherford in 1911 [Rut11] (based on the gold-foil experiment of H. Geiger and E. Marsden [Gei11]), the nuclear structure still draws many questions and presents itself in various, often unexpected ways. The vicinity of the closed proton nuclear shell $Z = 82$ is especially rich in these manifestations of the nuclear structure. To name few - the nuclear isomerism (first observed by Otto Hahn in ^{234}Pa [Hah21]), double and triple shape coexistence, first observed in ^{16}O [Mor56] and in ^{186}Pb [And00], respectively, or the exotic decay modes such as β -delayed fission [Kuz67a; Kuz67b].

For the production of exotic nuclei two methods are widely used. The isotope separation on-line (ISOL) method uses the bombardment of a thick target by particles with high energy, resulting in spallation, fission or fragmentation of the target nuclei. One of the most successful facilities employing this method is ISOLDE [Kug00] in CERN, Geneva. The second method of fusion-evaporation reactions uses bombardment of thin target with low energy projectiles. Reaction products leaving the target are separated by gas-filled or vacuum-mode separators, such as the velocity filter SHIP [Mün79], in GSI, Darmstadt.

The first part of the dissertation project is the investigation of the ^{186}Bi isotope and its α -decay daughter product ^{182}Tl with the use of $\alpha - \gamma$ decay spectroscopy. The studies of thallium and bismuth isotopes in the neutron-deficient side of the nuclide table revealed a multitude of phenomena linked to the near vicinity of the proton closed shell $Z = 82$. A systematic appearance of low-lying intruder states is ranked among the most interesting ones [Hey83; Hey87; Hey88; Woo92]. The $1/2^+$ ground state in the odd-mass thallium nuclei is caused by the valence $3s_{1/2}^{-1}$ proton $\pi(0p-1h)$ configuration, while the low-lying intruder $9/2^-$ state with $\pi(1p-2h)$ configuration is caused by the excitation of a proton across the $Z = 82$ gap to the $1h_{9/2}$ orbital. The situation in the even-mass thallium and bismuth nuclei is much more complex, due to the additional coupling of an unpaired neutron resulting in the multiplets of states. The multiplets can be both normal or intruder and can become isomeric states as well. A relatively small energy difference between the multiplets and/or the collective bands built on top of them can further complicate the studies.

Previous analysis of the $^{95}\text{Mo}(^{93}\text{Nb}, 2n)^{186}\text{Bi}$ [And03] and $^{97}\text{Mo}(^{92}\text{Mo}, p2n)^{186}\text{Bi}$

[Bat97] reactions revealed two isomeric states in ^{182}Tl populated after an α decay of ^{186}Bi with very similar half-lives. Only three γ transitions were identified in the former study and assigned to these isomers based on the energy balance of the observed transitions. Several other γ transitions remained unresolved and were not assigned to either of the isomers.

Data from the reaction $^{46}\text{Ti}(^{144}\text{Sm}, p3n)^{186}\text{Bi}$ measured at the velocity filter SHIP, Darmstadt, are available. A merger of the datasets from this and the aforementioned $^{95}\text{Mo}(^{93}\text{Nb}, 2n)^{186}\text{Bi}$ reactions increased the statistics of the collected data from the decay of ^{186}Bi about three times. The increased statistics allow us to extend the decay scheme and assign almost entire spectrum of the γ transitions following the α decay of ^{186}Bi with a use of prompt $\alpha - \gamma$ coincidences.

The effects of unpaired nucleons can be seen in the spectra of ^{186}Bi α -decay energies populating certain levels in ^{182}Tl . De-excitation transitions can be heavily converted and the α -decay energies may be summed up with the energies of the conversion electrons. The α -decay energy distributions corresponding to such γ transitions may be difficult to disentangle and interpret. The analysis of such distributions and an alternative interpretation of the excited states within ^{182}Tl will be described and employed.

The second aim of the project is the investigation of the cross section systematics in the fusion-evaporation reactions leading to neutron-deficient compound nuclei from the radon region. Investigation of rare and exotic demonstrations of the nuclear structure requires large amounts of collected data, often in millions of registered decays. However, the production of the neutron-deficient nuclei far away from the line of β -stability reaches its limits, thus reliable theoretical models predicting the yields of the measured reactions are crucial.

Nowadays, one of the most widely used model to estimate the cross sections of the fusion-evaporation reactions is the statistical code HIVAP [Rei81; Rei92]. As has been shown in the recent years, one of the parameters entering the calculation, fission barrier, is heavily reduced in the reactions leading to the neutron-deficient compound nuclei in the vicinity of the closed proton shell $Z = 82$ [And05]. The decrease of the barrier by around 30% causes the cross section to drop by several orders of magnitude. The dependence of the fission barrier scaling factor and mass of the compound nucleus is known from the bismuth and polonium neutron-deficient isotopes.

Smaller but still very significant decrease of the fission barrier is expected in radon and radium compound nuclei (around 27% for $^{199}\text{Rn}^*$, according to the mentioned systematics). However, up to this day no analysis focused on the evaluation of the cross sections in this region has been performed. Currently, data from the reactions leading to the neutron-deficient radon and radium isotopes are available. The reactions were measured at several projectile energies, which allows the establishment of the corresponding excitation functions. Through the variation of the parameters entering the theoretical

calculation, the predictions will be varied to fit the experimental results and the optimal set of the parameters will be extracted. One of these parameters, the aforementioned fission barrier scaling factor, will help to extend the systematics known from the polonium and bismuth isotopes.

The first chapter is dedicated to the theory behind the fusion-evaporation reactions and decays analysed in the project - alpha decay, gamma decay and internal conversion. The details about experimental setup - velocity filter SHIP and the detector system - are listed in the second chapter. The electronics and signal processing are presented therein, together with the description of the time-position correlation technique and the statistical analysis in case of poor statistics. The third chapter lists the goals and summary of previous studies concerning the main aims of the project. In the fourth chapter, preliminary results from the $\alpha - \gamma$ analysis of the decay data of ^{186}Bi are presented. The sixth chapter contains summary of the results and outlook.

Chapter 1

Physical background

1.1 Fusion-evaporation reactions

To this date, fusion-evaporation reactions (FER), which are also referred to as reactions of complete fusion or compound nucleus reactions, continue to be the sole method for producing nuclei that are much heavier than the ones involved in the reaction. The concept of the compound nucleus model was initially presented by N. Bohr in 1936 [Boh36] and subsequently enhanced by V. F. Weisskopf and D. H. Ewing in 1940 [Wei40].

During fusion-evaporation reactions, a projectile a with a kinetic energy¹ T_p , surpasses the fusion (Coulomb) barrier to merge with a target nucleus A . Once inside the target nucleus, the projectile's energy is distributed among all nucleons through two-body interactions until equilibrium is achieved. The result of this process is the formation of a compound nucleus (CN) characterized by high excitation energy (ranging from 20 to 60 MeV) and significant angular momentum ($60 - 80 \hbar$). The compound nucleus is typically created in a time frame of around 10^{-22} s [Lov06]. [If the excitation energy of the \$a + A\$ system significantly exceeds the fission barrier, quasi-fission can occur.](#)

The excessive excitation energy of the compound nucleus is radiated in the form of nucleons and/or α particles within a timespan of approximately $10^{-19} - 10^{-16}$ s. The deexcitation process of the excited compound nucleus is analogous to the evaporation of molecules from a hot liquid. The number of evaporated particles depends on the excitation energy, and the emission of each particle cools down the compound nucleus by roughly 10 MeV. Neutron evaporation channels (xn , where x denotes the number of evaporated neutrons) are usually predominant. In the neutron-deficient region, proton (pxn channel, involving one proton and x neutrons) and/or α (αxn channel, comprising one α particle and x neutrons) emission becomes favored due to the increase in neutron binding energies and a simultaneous decrease in proton binding energies.

The evaporation of a nucleon results in a relatively small reduction in angular mo-

¹All kinetic energies are in the laboratory frame throughout the work, unless stated otherwise

mentum. In case further nucleon evaporation would lead to states below the state of the nucleus with the minimal possible angular momentum for the given excitation energy (yrast line) further de-excitation occurs through discrete γ transitions. This process forms a yrast cascade, as illustrated in Fig. 1.1 and typically occurs over the interval of about $10^{-17} - 10^{-10}$ s. The final de-excited product, in the ground (or isomeric) state, is referred to as an evaporation residue (ER).

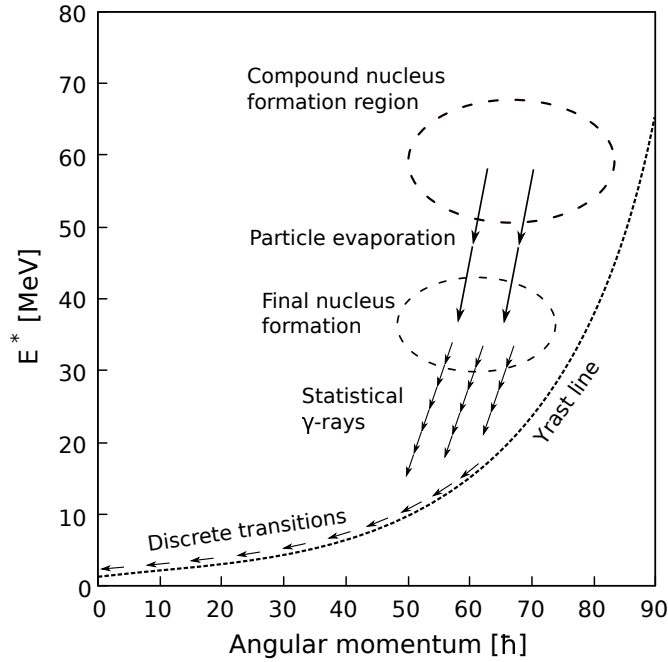


Figure 1.1: Process of particle and γ evaporation from the excited compound nucleus.

The process of the fusion-evaporation reactions can be schematically written as:



where B represents evaporation residue and evaporated particles are stated as b . Simplified notation of the reaction is $A(a,b)B$. A visual representation of the process is in Fig. 1.2.

The energy balance of the reaction can be expressed via amass of a projectile m_p , a target m_T and an excited CN m_{CN}^* and kinetic energy of the projectile T_p and the CN T_{CN} :

$$(m_p + m_T)c^2 + T_p = m_{CN}^*c^2 + T_{CN} \quad (1.1)$$

Since the momentum of the projectile $|\vec{p}_p|$ is equal to the momentum of the CN $|\vec{p}_{CN}|$ (conservation of momentum), the kinetic energy of the CN can be expressed as

$$T_{CN} = \frac{p_{CN}^2}{2m_{CN}^*} = \frac{m_p}{m_p} \frac{p_{CN}^2}{2m_{CN}^*} = \frac{m_p}{m_{CN}^*} \frac{p_p^2}{2m_p} = \frac{m_p}{m_{CN}^*} T_p \quad (1.2)$$

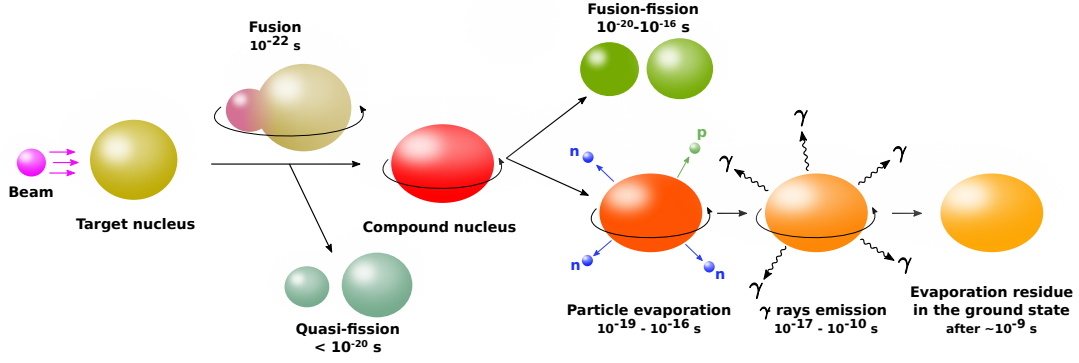


Figure 1.2: Visualisation of the fusion-evaporation reactions.

Combining equations 1.1 and 1.2, the expression for the mass of the excited CN is

$$m_{CN}^* c^2 = (m_p + m_T) c^2 + T_p \left(1 - \frac{m_p}{m_{CN}^*} \right) \quad (1.3)$$

An approximation $m_{CN}^* = m_p + m_T$ can be done for $m_{CN}^* \gg m_p$. Then

$$m_{CN}^* c^2 = (m_p + m_T) c^2 + T_p \left(1 - \frac{m_p}{m_p + m_T} \right) = (m_p + m_T) c^2 + T_p \left(\frac{m_T}{m_p + m_T} \right) \quad (1.4)$$

and the excitation energy of the CN is

$$E_{CN}^* = (m_{CN}^* - m_{CN}) c^2 = (m_p + m_T - m_{CN}) c^2 + T_p \left(\frac{m_T}{m_p + m_T} \right) \quad (1.5)$$

The term $(m_p + m_T - m_{CN}) c^2$ represents the Q value of the reaction and comes from the difference of binding energies. The kinetic energy of the projectile is represented by the $T_p m_T / (m_p + m_T)$ term.

The energy spectrum of the evaporated neutrons (in Fig. 1.3) can be expressed as

$$N(\varepsilon) d\varepsilon = \frac{\varepsilon}{T^2} \exp \left(\frac{-\varepsilon}{T} \right) d\varepsilon \quad (1.6)$$

The nuclear temperature T is given by

$$E^* = aT^2 - T \quad (1.7)$$

where E^* is the excitation energy of the nucleus and a is the level density parameter $A/12 - A/8$ from the Fermi gas model [Lov06] .

The most probable energy of the neutrons is T and the average energy is $2T$. Evaporation of a charged particle (proton and/or α) requires non-zero kinetic energy ε_s (unlike evaporation of a neutron), which determines a minimal kinetic energy of the particle. This threshold energy is approximately equal to the Coulomb barrier. The energy spec-

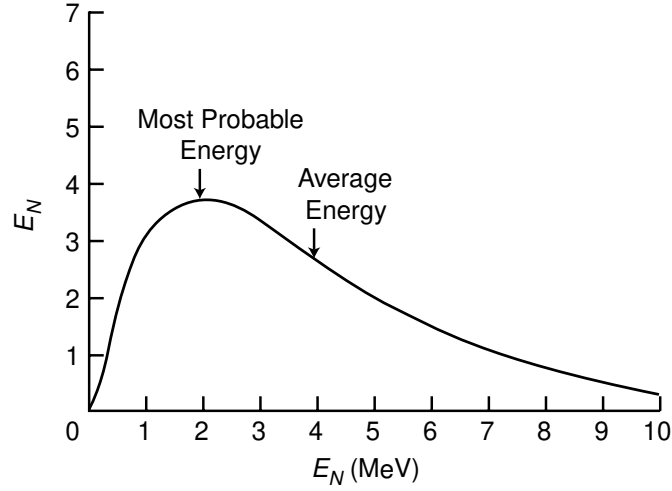


Figure 1.3: The energy spectrum of neutrons emitted from the excited compound nucleus [Lov06].

trum of the evaporated particles is then

$$N(\varepsilon) d\varepsilon = \frac{\varepsilon - \varepsilon_s}{T^2} \exp\left(\frac{-\varepsilon - \varepsilon_s}{T}\right) d\varepsilon \quad (1.8)$$

1.1.1 Cross section of the fusion-evaporation reaction

An important feature of the FERs is that the probability of the production of a certain ER (cross section of the reaction) is independent of the way CN was formed². The hypothesis was experimentally confirmed by S. N. Ghoshal [Gho50] by producing the compound nucleus $^{64}\text{Zn}^*$ in $^{63}\text{Cu} + p$ and $^{60}\text{Ni} + \alpha$ reactions. The ratios between the cross sections $\sigma(\alpha, n) : \sigma(\alpha, 2n) : \sigma(\alpha, pn)$ for ^{60}Ni target agreed with those of $\sigma(p, n) : \sigma(p, 2n) : \sigma(p, pn)$ for ^{63}Cu target. Excitation functions³ from this experiment are in Fig. 1.4.

The independence of the entrance and exit channels of the FERs allows us to express the cross section of $a + A \rightarrow \text{CN}^* \rightarrow b + B$ reaction as

$$\sigma(a, b) = \sigma_{\text{CN}}(a, A) P_b(E) \quad (1.9)$$

where $\sigma_{\text{CN}}(a, A)$ represents the cross section (probability) of the creation of the compound nucleus and $P_b(E)$ is the probability that CN with excitation energy E decays by evaporation of particle(s) b .

²Also known as Bohr independence hypothesis or the amnesia assumption

³Dependence of the reaction cross section on the excitation energy of the CN/energy of the incident projectile

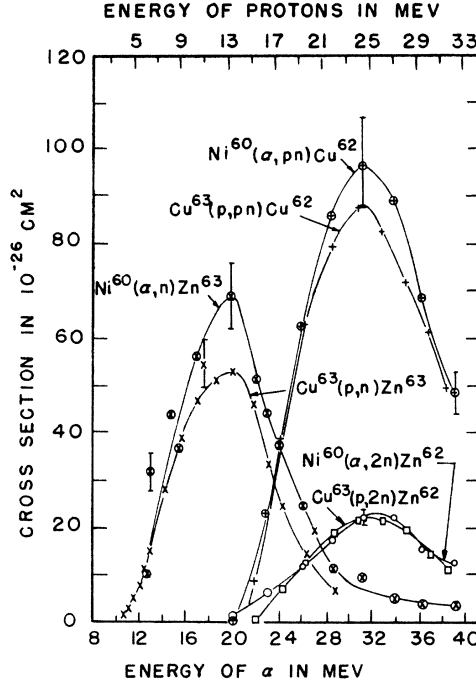


Figure 1.4: Experimental excitation functions of $^{63}\text{Cu} + p \rightarrow ^{64}\text{Zn}^*$ and $^{60}\text{Ni} + \alpha \rightarrow ^{64}\text{Zn}^*$ reactions from [Gho50]

Experimental cross section

Total number of ERs produced in the reaction (N_{Re}) is proportional to the cross section of the reaction (σ), the number of the projectiles (N_p) and the area density of the nuclei in the target per area unit (η):

$$N_{ER} = \sigma N_p \eta \quad (1.10)$$

An area density is

$$\eta = f \frac{N_T}{S} \quad (1.11)$$

where f is the ratio of desired target nuclei to the total number of nuclei in the target (known as the isotopic purity), N_T is the number of nuclei in the target with an area S . Further, $N_T = \frac{m}{M_m} N_A$ where m is the mass of the target, M_m is the molar mass of the target nuclei and N_A is the Avogadro constant.

The number of observed decays N_i originating from the ERs is lower than the total number of ERs produced in the reaction. Detector efficiency ε_i for the detected particles (see section 2.3), transmission of the SHIP separator ε (see section 2.2 and Fig. 2.2) and branching ratio of the corresponding decay must be considered as well. Relation between N_{ER} and N_i is

$$N_i = b_i \varepsilon_i \varepsilon N_{ER} \quad (1.12)$$

The total number of ERs produced in the reaction is then

$$N_{ER} = \sigma N_p f \frac{N_T}{S} = \sigma N_p f \frac{m}{S} \frac{N_A}{M_m} = \sigma N_p f d \frac{N_A}{M_m} = \frac{N_i}{b_i \varepsilon_i \varepsilon} \quad (1.13)$$

where $d = m/S$ is the width of the target in g/cm² and M_m/N_a represents an atomic mass of the target nucleus.

The total number of projectiles is derived from the charge collected by a Faraday cup Q divided by the charge state of the projectiles q and elementary charge e . The total collected charge can be expressed in terms of the total charge collection time t and an average beam current \bar{I} or a beam current during the pulse I and the duty factor D , reflecting pulse-regime of the accelerator (as a ratio between a pulse time and a total macropulse duration):

$$N_p = \frac{Q}{qe} = \frac{\bar{I}t}{qe} = \frac{IDt}{qe} \quad (1.14)$$

In the experiments performed at the SHIP, the beam intensity is measured in Scale Coulomb Counter units (SCC). The value of beam current changes throughout the experiment, therefore SCC unit and the SCC counting rate R is used. Charge collection time t is then given as

$$t = \frac{SCC}{R} \quad (1.15)$$

and the total number of projectiles can be expressed as

$$N_p = SCC \frac{ID}{Rqe} \quad (1.16)$$

Finally, from the combination of equations 1.13 and 1.16, the experimental cross section of the reaction is

$$\sigma = \frac{1}{fd} \frac{M_m}{N_A} \frac{N_i}{b_i \varepsilon_i \varepsilon} \frac{R}{SCC} \frac{qe}{ID} \quad (1.17)$$

Statistical code Hivap

Firstly introduced by W. Reisdorf [Rei81; Rei92] as a modification of the GROGI code [Gro67] - fission channel was incorporated into the de-excitation phase of the FER. The fusion cross section is calculated via the summation of the partial waves as follows

$$\sigma_{fus}(E) = \pi \lambda^2 \sum_{l=0}^{L_{crit}} (2l+1) T_l(E) \quad (1.18)$$

where λ is the reduced wavelength of the entrance channel and $T_l(E)$ are the transmission coefficients of the penetrating waves. The critical value L_{crit} of the angular momentum

quantum number l emerges from the rapid decrease of the survival probability of the CN with increasing angular momentum. The typical values are $L_{crit} \sim 20$ for mercury ($Z = 80$) and up to $L_{crit} \sim 30$ for radium isotopes ($Z = 88$) [Qui93].

In the presented study, two different models are utilized to determine the values of $T_l(E)$. The first model, referred to as the inverted parabola (IP) approach, approximates the Coulomb plus nuclear force near its maximum using a parabola with a curvature of $\hbar\omega_l$ and a height of B_l [Vaz81]. The transmission coefficients can then be obtained from the Hill-Wheeler formula [Hil53]:

$$T_l(E) = \frac{1}{1 + \exp[(2\pi/\hbar\omega)(B_l - E)]} \quad (1.19)$$

The IP approach has been found to be effective above the semi-empirical Bass barrier [Bas77; Bas80], while fusion below the barrier is significantly suppressed. To account for the sub-barrier fusion, an alternative approach known as barrier fluctuations (BF) is employed. In this approach, the fusion barrier is considered to fluctuate with a Gaussian distribution characterized by a height of B_0 and a standard deviation of $\sigma(B_0)$. The values of the barrier fluctuation are discussed in [Qui93] (see Fig. 12 and the accompanying description), where values of 2.5 and up to 3.5 are used for spherical and deformed compound nuclei, respectively. The BF approach has been shown to accurately reproduce cross section values above the fusion barrier as well [And05], in good agreement with the IP approach.

The de-excitation part of the calculation employs the evaporation theory and considers the competition between fission, γ ray, α -particle, and nucleon emission. The ratio of nuclear level densities (a_f/a_n) is calculated as described in [Rei92]. The damping constant is used to represent the fading of the shell effects on the level density [Ign75]. Another crucial parameter, the fission barrier, is calculated using the following equation:

Table 1.1: Values of HIVAP parameters used throughout this work, majority according to [Rei90]. Parameters used with values equal to zero are not listed.

Parameter	Description	Value
LEVELPAR	Scale parameter for the level density	1.16
a_f/a_n	Level density ratio	1
BARFAC	Fission barrier scaling	variable
EDAMP	Shell effect damping constant [MeV]	18.5
V0	Strength parameter of nuclear potential[MeV]	59
R0	Radius parameter [fm]	eq. 15 in [Rei85]
D	Diffuseness parameter [fm]	0.75
Q2	Quadrupole moment of target nucleus [fm ²]	β_2 from [Möl16]
CRED	Barrier thickness parameter	1
SIGR0	Barrier fluctuation $\sigma(B_0)$ [% of R0]	~2.5 for spherical nuclei up to ~ 3.5 for deformed nuclei

$$B_f = BF \times B_f^{RLD} - \Delta W_{gs} \quad (1.20)$$

where BF is a free scaling parameter and B_f^{RLD} is the fission barrier according to the rotating liquid drop model [Coh74]. The ground state correction $\Delta W_{gs} = M_{exp} - M_{LD}$ represents the difference between the experimental and theoretical masses from the liquid-drop model. The values of the HIVAP parameters used in the calculations are summarized in Table 1.1.

1.2 Other types of reactions

transfer, spallation,

1.3 Nuclear decays

The stability of atomic nuclei is characterized by an equilibrium between the number of protons and neutrons. To date, out of approximately 3300 known nuclides only 252 have never been observed to decay and are therefore considered stable. The unstable nuclei can decay either by β decay - a proton is transformed into a neutron or vice versa, or directly emitting protons, neutrons, α particles or by fission. Less common decays are, for example, double β /electron capture decays, β -delayed fission, cluster emission, and others. Studying the decay modes and their characteristic properties gives valuable information about the nuclear structure and the forces acting within the nuclei. In this section, we will provide a detailed explanation of the decays relevant to this work.

1.3.1 Alpha decay

Alpha decay occurs when the Coulomb force, which increases with the squared atomic number of a nucleus ($\sim Z^2$), overcomes the attractive nuclear force, which increases with the mass of a nucleus ($\sim A$). Such unbalance leads to the emission of an α particle (helium nucleus), consisting of two protons and two neutrons strongly bound together. In heavy nuclei, α decay becomes energetically possible and it is the preferred mode of decay. The process of an α decay in a nucleus with mass number A , atomic number Z , and neutron number N can be represented schematically as

$${}^A_ZX_N \longrightarrow {}^{A-4}_{Z-2}Y_{N-2} + {}^4_2\text{He}^{2+} + Q_\alpha \quad (1.21)$$

where Q_α represents the energetic balance of the reaction and can be expressed in terms of binding energies B as

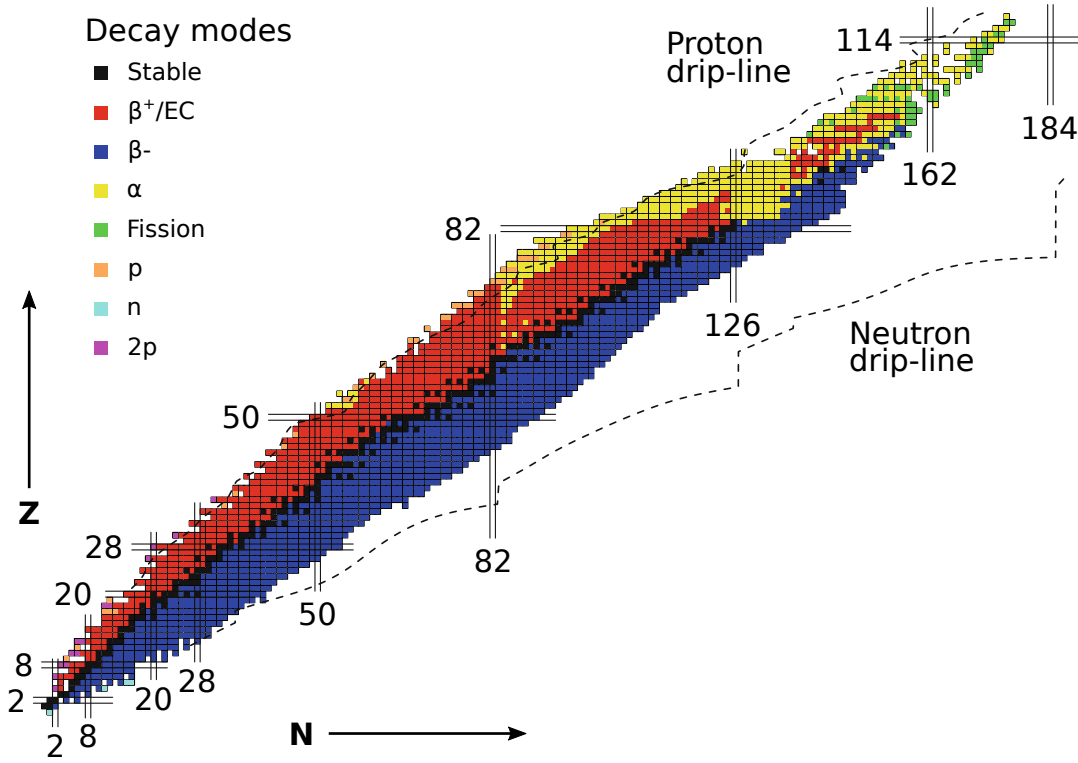


Figure 1.5: Nuclear chart showing experimentally observed nuclei. Figure adapted and modified from Ref. [Tan23].

$$Q_\alpha = [B({}_{Z-2}^{A-4}Y) + B(\alpha)] - B({}_Z^AX) \quad (1.22)$$

The Q_α value is positive (exothermic) for spontaneous α decay and typically ranges from around 4 up to 12 MeV. The energy released in a decay is transformed into the kinetic energies of the daughter nucleus (E_D , also referred to as the recoil energy) and the escaping α particle (E_α). The nuclear mass of a nucleus is $M({}_Z^AX) = Zm_p + Nm_n - B({}_Z^AX)$, therefore the Q value of an α decay can be expressed in terms of nuclear masses (or mass deficits instead) as well:

$$Q_\alpha = [m({}_Z^AX_N) - m({}_{Z-2}^{A-4}Y_{N-2}) - m(\alpha)]c^2 = E_D + E_\alpha \quad (1.23)$$

Applying the laws of energy and momentum conservation on the equation 1.23, the Q value can be calculated as

$$Q_\alpha = E_\alpha \frac{m({}_{Z-2}^{A-4}Y_{N-2}) + m(\alpha)}{m({}_Z^AX_N)} \approx E_\alpha \frac{A}{A-4} \quad (1.24)$$

and similarly, the kinetic energy of the daughter nucleus is

$$E_D = Q_\alpha - E_\alpha \approx E_\alpha \frac{A}{A-4} - E_\alpha = E_\alpha \frac{4}{A-4} \quad (1.25)$$

For a nucleus with $Z \approx 200$, an α particle carries around 98% of the released energy and

only around 2% is transformed into the recoil kinetic energy of the daughter nucleus.

The initial theory of α decay proposed that an α particle is formed within the nucleus prior to the decay [Gam28; Gur28]. This pre-formed α particle encounters a potential barrier that prevents its spontaneous emission from the nucleus. The height of this barrier can be determined using Coulomb's law, which is approximately 28 MeV for ^{238}U , while the energy of the emitted α particles is around 4.2 MeV. According to classical mechanics, the emission of such α particles would be impossible. However, quantum mechanics allows for the possibility of an α particle to tunnel through the barrier with a certain probability. The emission of an α particle is the most favorable and efficient method of energy release due to its relatively high binding energy of ~ 28.3 MeV.

Because of the α -particle tunneling through the potential barrier, the half-life of the α decay is heavily dependent on the Q_α value. H. Geiger and J. M. Nuttall found a linear dependence between the logarithm of the decay constant and the range (and thus energy) of α particles [Gei11]. Later, this dependence became known as the Geiger-Nuttall law:

$$\log T_{1/2} = a(Z) + \frac{b(Z)}{\sqrt{Q_\alpha}} \quad (1.26)$$

The variables $a(Z)$ and $b(Z)$ vary for each isotopic series. There are several available theoretical approaches for partial α decay half-life determination, such as the model presented in [Poe80] with the set of updated parameters from [Poe06] or alternatively an approach described in [Qi09], which can be used also for the cluster emission half-life.

Another factor influencing the half-life of the α decay is the angular momentum change between the initial (I_i) and final (I_f) nucleus. The total spin of an α particle is zero, due to the arrangement of four constituent nucleons. The angular momentum carried away by the α particle after the decay is therefore purely of orbital character. Possible angular momentum values can be $|I_i - I_f| \leq L_\alpha \leq |I_i + I_f|$. The parity change is given by the selection rule given by the parity conservation: $\pi_i = (-1)^{L_\alpha} \pi_f$. Therefore, if the parity of the initial and final state are the same, L_α must be even and if the parities are opposite, L_α must be odd.

The α transitions between the same states (regarding angular momenta and parities) are strongly preferred. The more the states differ, the more the transitions between them are retarded. The hindrance factor (HF) evaluates the extent to which the experimentally measured transition is slower compared to an unhindered, theoretical prediction:

$$\text{HF} = \frac{T_{1/2, \text{exp}}}{T_{1/2, \text{theor}}} \quad (1.27)$$

Another method to calculate the hindrance factor of an α decay is to compare reduced α decay widths of a certain transition δ^2 with unhindered (usually ground state (g.s.) \rightarrow ground state) transitions in neighbouring even-even nuclei δ_{e-e}^2 :

$$\text{HF} = \frac{\delta_{e-e}^2}{\delta^2} \quad (1.28)$$

The reduced width of an α decay represents the decay stripped of the strong dependence on the decay energy. Reduced width is directly linked to the α decay probability as

$$\lambda_\alpha = \frac{\delta^2 P}{\hbar} \quad (1.29)$$

where P is the barrier penetration factor and defines the probability of an α particle to penetrate the potential barrier. The penetration probability of an α particle carrying angular momentum L after an α decay with a Q value was derived by J. O. Rasmussen [Ras59]. The natural logarithm of the factor P has been shown to be twice the Wentzel-Kramers-Brillouin integral

$$\ln P = -2 \frac{\sqrt{2m}}{\hbar} \int_{R_i}^{R_o} \left[V(r) + \frac{2Ze^2}{r} + \frac{\hbar L(L+1)}{2mr^2} - Q \right]^{\frac{1}{2}} \quad (1.30)$$

where R_i and R_o are the inner and outer classical turning points (simplified, R_i is the nuclear radius and R_o is the distance at which an α particle leaves the nucleus). Factor m is the reduced mass of an α particle and a daughter nucleus (with atomic number Z). The potential $V(r)$ is

$$V(r) = -1100 \exp\left(-\frac{r - 1.17A^{1/3}}{0.574}\right) \text{MeV} \quad (1.31)$$

Based on the HF values, α transitions can be summarized as follows (according to [Lov06]):

- HF = 1 – 4: favored transition. The populated states within mother and daughter nuclei are the same ($I_i^{\pi_i} = I_f^{\pi_f}$). Within odd A nuclei, favored transitions usually lead to the excited daughter product, since the α particle is formed from a pair of nucleons from a lower-lying level.
- HF = 4 – 10: transition between mixed or overlapping states.
- HF = 10 – 100: transition with parallel initial and final spin projections, however, the wave function overlap is not favorable.
- HF = 100 – 1000: transition between the states with parallel spin projections but with opposite parities.
- HF > 1000: transition between the states with antiparallel spin projections and opposite parities.

1.3.2 Internal transitions

Nuclear decays and nuclear reactions often populate states energetically above the ground state in the final nucleus. These excited states are usually promptly de-excited to the ground or other excited states by internal transitions, that is either γ ray emission or internal conversion.

Emission of γ rays

The excited states of nuclei tend to promptly emit one or more photons to reach a more energetically favorable configuration. The energy range of the emitted photons can be from a few keV up to several MeV. In general, the energy balance of the emission of a photon with energy E_γ is

$$\Delta E = E_\gamma + T_N \quad (1.32)$$

where $\Delta E = E_i - E_f$ is the energy difference between the initial and the final state of the nucleus. The recoil energy of the nucleus T_N emerges from the conservation of linear momentum - the sum of the momenta of the nucleus and the emitted photon is zero ($\vec{p}_N + \vec{p}_\gamma = 0$). The recoiling nucleus (with mass M) is non-relativistic, therefore the kinetic recoil energy can be expressed as

$$T_N = \frac{p_N^2}{2M} = \frac{p_N^2 c^2}{2Mc^2} = \frac{p_\gamma^2 c^2}{2Mc^2} = \frac{E_\gamma^2}{2Mc^2} \quad (1.33)$$

For example, the recoil energy for 1 MeV photon emitted from the nucleus with $A=200$ is only ~ 3 eV, therefore in the cases of nuclear decay spectroscopy it is completely negligible since typical experimental resolutions of the detectors are in order of keV.

Discrete nuclear levels are described by their spin, parity, and excitation energy. The γ -ray emission is controlled by the conservation of energy and angular momentum and provides a large amount of information on the structure of nuclei. The angular momentum carried away by the γ ray with a quantum number L is determined by the momentum conservation as

$$|I_i - I_f| \leq L \leq |I_i + I_f| \quad (1.34)$$

where I_i and I_f are spin and quantum numbers of the initial and final levels, respectively. The multipole order of the transition is defined by the L quantum number: dipole for $L=1$, quadrupole for $L=2$, octupole for $L=3$, etc. Additionally, the parity of the γ ray depends on the angular momentum and the electric (E) or magnetic (M) character of the transition and is given as

$$\begin{aligned}\Delta\pi(EL) &= (-1)^L \\ \Delta\pi(ML) &= (-1)^{L+1}\end{aligned}\tag{1.35}$$

Consequently, the states with the same parity can be connected either by the even- L electric or odd- L magnetic transition, while the deexcitation between opposite parity states can proceed by even- L magnetic or odd- L electric γ -ray emission. In general, EL and ML are called the multipolarity of the γ radiation and of the transition.

The lowest possible multipolarity of the transitions between $I_i=I_f$ states is a dipole transition with $L=1$. There are no monopole ($L=0$) transitions in which a single photon is emitted (classically, the monopole moment is the electric charge, which is static over time). For $I_i=I_f=0$ states the selection rules only allow a transition with $L=0$. In this case, the excited states decay through internal conversion, described in the following Sec. 1.3.2.

The rate (or the probability) of the transition heavily depends on its energy, character, and multipolarity and can be calculated using the following Weisskopf single-particle estimates [Wei51]:

$$\begin{aligned}\lambda_E(L) &\cong \frac{4.4(L+1)}{L[(2L+1)!!]^2} \left(\frac{3}{L+3}\right)^2 \left(\frac{E_\gamma}{197 \text{ MeV}}\right)^{2L+1} R^{2L} \times 10^{21} \text{ s}^{-1} \\ \lambda_M(L) &\cong \frac{1.9(L+1)}{L[(2L+1)!!]^2} \left(\frac{3}{L+3}\right)^2 \left(\frac{E_\gamma}{197 \text{ MeV}}\right)^{2L+1} R^{2L-2} \times 10^{21} \text{ s}^{-1}\end{aligned}\tag{1.36}$$

where the nuclear radius $R = 1.25A^{\frac{1}{3}}$ is in 10^{-15} m and E_γ is in MeV. The ratio between electric and magnetic transition decay constants is

$$\frac{\lambda_E}{\lambda_M} \approx 2.32R^2 \approx 2.9A^{\frac{2}{3}}\tag{1.37}$$

The properties of the transition probabilities via γ ray emission can be summarized as follows:

- The probability heavily depends on the energy of the transition. An increase of the energy by one order increases the probability by three orders and vice versa.
- Transitions with lower multiplicities are dominant. The probability of 100 keV transition of $E1$ is around five orders of magnitude higher than for $E2$ transition (for nuclei with $A \approx 200$).
- For a given energy and multipolarity, the electric transition probability is around two orders of magnitude higher than that of magnetic transition. Therefore, in the $M2$ transition, a small admixture of $E1$ can be present.

The ratio between theoretical estimate from equation 1.36 and experimentally measured value gives the transition probability in Weisskopf units (W. u.) [Fir96]:

$$B(EL|ML) = \frac{\lambda_W(EL|ML)}{\lambda_{Exp}(EL|ML)} \quad [\text{W. u.}] \quad (1.38)$$

Internal conversion

Along the de-excitation via the γ ray emission, an excited nucleus can undergo a process called internal conversion (IC). The interaction between the electromagnetic multipole fields of the nucleus and the atomic electron orbitals via the Coulomb force and the transferred energy can cause one of the electrons to be emitted. The energy of the emitted electron depends on the binding energy B_e needed to release the electron from the atomic orbital and the energy of the transition ΔE :

$$E_e = \Delta E - B_e \quad (1.39)$$

The binding energy of the electron in a particular shell therefore represents the threshold energy of the IC process. The conversion electrons (CE) are labeled according to the shell they were emitted from - K , L , M ,... corresponding to the principal atomic quantum numbers $n = 1, 2, 3 \dots$

After the emission of a conversion electron, the vacant place on the orbital is filled rapidly with an electron from the outer orbitals. The relocation of the electron from one shell to another causes the emission of X-rays which are characteristic for each element. The energy of the characteristic X-rays is given as the difference between the energies of the initial and final electron shells. Individual electron orbitals within the shell have slightly different binding energies. For example, the L shell ($n = 2$) consists of $2s_{1/2}$, $2p_{1/2}$, and $2p_{3/2}$ orbitals and the conversion electrons originating from these orbitals are referred to as L_1 , L_2 , and L_3 conversion electrons, respectively. Characteristic X-rays are therefore different for the electron relocations between $K-L_1$, $K-L_2$, and $K-L_3$ orbitals and are noted as K_{α_3} , K_{α_2} and K_{α_1} X-rays, respectively. A summary of the notations of the characteristic X-rays is in table 1.2 together with thallium X-ray energies and intensities as an example.

In the lead region, the X-ray intensities (and ratios between them) tend to not change significantly between the elements, therefore they are very similar to those of thallium from table 1.2. For 100 K -shell vacancies, K_{α_1} X-rays are the most intense with $\sim 46\%$ intensity, followed by K_{α_2} with $\sim 27 - 28\%$, L_{α_1} with $\sim 12 - 14\%$, K_{β_1} with $\sim 11\%$ etc.

The intensity of the emitted conversion electrons heavily depends on the multipolarity of the radiation. In some cases, the de-excitation of the excited states proceeds nearly exclusively via internal conversion, in others it is almost negligible compared with γ ray emission. In the transition probability calculations, both processes have to be considered.

Table 1.2: Notation for the characteristic X-ray transitions. Siegbahn notation was first introduced in Ref. [Sie16]. Reference energies of X-ray transitions in thallium are from Ref. [Fir96]. The intensities are given per 100 K -shell vacancies.

Classical (Siegbahn) notation	Final – initial shell	X-ray energies in thallium [keV] (Intensity [%])
K_{α_1}	$K - L_3$	72.87 (46.2)
K_{α_2}	$K - L_2$	70.83 (27.6)
K_{α_3}	$K - L_1$	70.18 (0.0395)
K_{β_1}	$K - M_3$	82.57 (10.7)
K_{β_2}	$K - N_2N_3$	84.87 (3.9)
\vdots	\vdots	\vdots
L_{α_1}	$L_3 - M_5$	10.27 (12.4)
L_{α_2}	$L_3 - M_4$	10.17 (1.39)
\vdots	\vdots	\vdots

Therefore, the total decay probability of the excited state is

$$\lambda = \lambda_\gamma + \lambda_{IC} \quad (1.40)$$

where λ_γ and λ_{IC} are the decay probabilities of γ ray emission and internal conversion, respectively. By defining the internal conversion coefficient (ICC)

$$\alpha = \frac{\lambda_{IC}}{\lambda_\gamma} \quad (1.41)$$

The total decay probability can be further expressed as

$$\lambda = \lambda_\gamma(1 + \alpha) \quad (1.42)$$

The decay probability of the IC is the sum of partial probabilities of the conversion on each shell $\lambda_{IC} = \lambda_{IC,K} + \lambda_{IC,L} + \lambda_{IC,M} + \dots$ and the total decay probability is then

$$\lambda = \lambda_\gamma + \lambda_{IC,K} + \lambda_{IC,L} + \lambda_{IC,M} + \dots = \lambda_\gamma(1 + \alpha_K + \alpha_L + \alpha_M + \dots) \quad (1.43)$$

The following equations from [Kra88] give the estimate for the conversion coefficients of electric (E) and magnetic (M) multipole transitions in a nucleus with an atomic number Z :

$$\begin{aligned}\alpha(EL) &\cong \frac{Z^3}{n^3} \left(\frac{L}{L+1} \right) \left(\frac{e^2}{4\pi\epsilon_0\hbar c} \right)^4 \left(\frac{2m_e c^2}{E} \right)^{L+5/2} \\ \alpha(ML) &\cong \frac{Z^3}{n^3} \left(\frac{e^2}{4\pi\epsilon_0\hbar c} \right)^4 \left(\frac{2m_e c^2}{E} \right)^{L+3/2}\end{aligned}\tag{1.44}$$

where n is the principal quantum number of the bound electron wave function and the term $e^2/(4\pi\epsilon_0\hbar c)$ is the fine structure constant with a value of about 1/137. Theoretical values of conversion coefficients can be evaluated using a tool BRICC [Kib08].

The ICC of the transition can be determined from the number of experimentally measured γ rays N_γ and conversion electrons N_{CE} (corrected by the detection efficiency of the corresponding detector):

$$\alpha = \frac{N_{CE}}{N_\gamma}\tag{1.45}$$

In general, the properties of the internal conversion coefficients can be summarized as follows:

- The IC is significantly more probable in heavy nuclei than in the lighter ones due to Z^3 dependence.
- The probability of the IC decreases with the increasing energy of the transition.
- The ICCs increase rapidly with the increasing transition multipolarity.
- For a given transition, the ratio between K and L conversion electron intensities is around 8, since the conversion on higher atomic shells decreases like $1/n^3$.

1.4 Nuclear isomerism

In addition to the lowest energy state, the ground state, a nucleus may also exist in a metastable excited state known as an isomer. First concept of nuclides having more than one configuration proposed by F. Soddy [Sod17].

Three different types of isomerism occur when the isomer's decay is hindered by a large change in a physical property of the nucleus - a large change in the magnitude or the direction of the angular momentum (spin and K isomers, respectively) or a large change in the shape of the nucleus.

- **Spin isomers** - a large change in the magnitude of the angular momentum
- **K isomers** - a large change in the direction of the angular momentum
- **Shape isomers** - a significant change in the shape of the nucleus

An isomer can be described as a secondary minimum in the potential energy, where the nucleus gets trapped before decaying to the ground state, as is schematically depicted in Fig. 1.6.

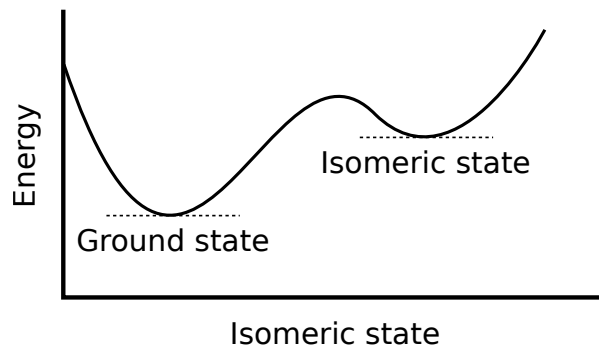


Figure 1.6: Caption

1.4.1 Types of nuclear isomers

spin, K, shape

1.5 Methods for nuclear structure studies

1.5.1 Decay spectroscopy

alpha decay spectro, beta decay spectro etc

1.5.2 Laser spectroscopy

e.g. ISOL methods, ISOLDE

1.5.3 In-beam spectroscopy?

Chapter 2

Experimental Background

In this chapter, a description of the Separator for Heavy Ion reaction Products (SHIP) and detection system will be presented. Electronic systems, signal processing, and correlation techniques will be explained as well.

2.1 Experimental production of nuclei

A beam of projectiles is provided by UNiversal Linear ACcelerator (UNILAC), which can accelerate elements up to uranium ($Z = 92$) to energies up to 20 AMeV (MeV per nucleon). Accuracy of the beam energy is ± 0.01 AMeV and beam intensities can reach 3 pμA for $^{40}\text{Ar}^{8+}$, 1.2 pμA for $^{58}\text{Fe}^{8+}$ and 0.4 pμA for $^{82}\text{Se}^{12+}$ (1 pμA (particle micro Ampere) = 6.24×10^{12} particles/s) [Hof00]. UNILAC operates in a pulse mode with 50 Hz frequency - one 20 ms macro-pulse consists of ~ 5 ms irradiation period (beam-on) and ~ 15 ms pause period (beam-off).

Accelerated beam is focused onto a target to the spot with a diameter of 5–10 mm [Fol95; Lom02]. The target consists of eight banana-shaped segments, each with dimensions 110×23 mm, arranged into a circle with a diameter of 310 mm. The target material is evaporated onto a carbon foil about $35 \mu\text{g}/\text{cm}^2$ thin and covered with another $10 \mu\text{g}/\text{cm}^2$ carbon layer, to decrease sputtering and increase target emissivity. The targets are $(0.1 - 1) \text{ mg}/\text{cm}^2$ thick, for lead and bismuth targets it is usually $\approx 500 \mu\text{g}/\text{cm}^2$. A thicker target leads to wider excitation functions (due to a larger distribution of energy losses of the projectiles in the target) which subsequently leads to the mixing of different evaporation channels and thus a higher background.

Projectiles can pass through inhomogeneities and pinholes in the target and increase background in the detector system. A movable $(30 - 60) \mu\text{g}/\text{cm}^2$ carbon foil (also called charge-equilibration foil) is therefore placed ~ 20 cm behind the target. The foil equilibrates the charge state of the reaction products and projectiles since the separator is optimized for particles with a particular charge state, while other states are suppressed.

Since melting points of typical target materials are often low (for example, lead melts at 327.5 °C and bismuth melts at 271.3 °C), rotating target wheels are used to spread the deposited energy. The target wheel rotates synchronously with the beam macro-pulse structure at 18.75 Hz. Therefore, every third target segment is hit while the next two segments are skipped. The same target segment is then irradiated after a 160-ms cooling period (three full wheel rotations). Target material can also be in the form of a compound to increase its melting point, such as PbS or Bi₂O₃.

2.2 Nuclei separation - SHIP

Separator for Heavy Ion reaction Products (SHIP) located at GSI Darmstadt (Germany), is an electromagnetic separator, which uses kinematic properties of evaporation residues (ER) to separate them from other reaction products and projectiles based on their velocity [Mün79; Hof00]. Configuration of the SHIP (Fig. 2.1) can be written as $3Q, E, 2M, 2M, E, 3Q, M$, where Q is a magnetic quadrupole, E is an electric deflector and M is a dipole magnet. In principle, SHIP consists of two velocity filters ($E, 2M$) facing each other. In contrast to the classical Wien filter, SHIP has separated electric and magnetic fields, which improves its efficiency and background suppression.

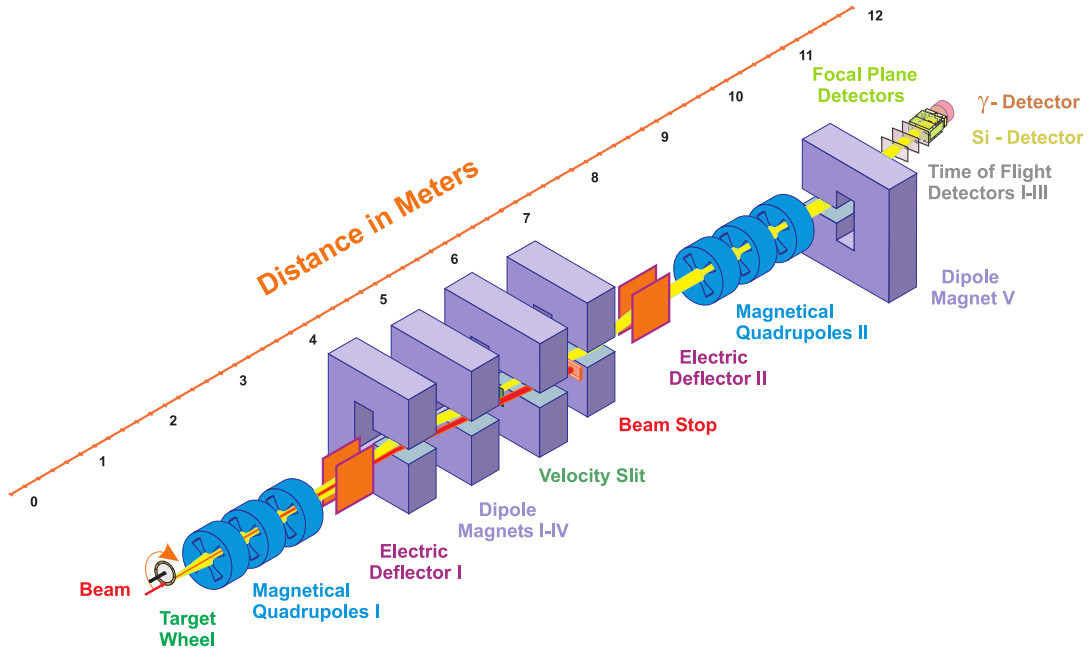


Figure 2.1: Velocity filter SHIP at GSI Darmstadt.

After the irradiation of the target, reaction products leave the target scattered at different angles. The focusation behind the target is done by the electro-magnetic lenses arranged as quadrupole triplet. Each magnet is turned by 120°, to ensure a uniform focusation. Afterwards, particles enter the ion-optical separator, where electric and

magnetic fields perpendicular to each other interact on the charged particles by the Lorentz force:

$$F = qE + qvB$$

To pass the filter without deflection, Lorentz force has to be 0, therefore $qE = qvB \rightarrow E/B = v$. This allows for charged particles with a certain velocity to pass the filter independently on their charge. Since the target nuclei are at rest and therefore have zero momentum, the momentum of an ER is the same as that of a projectile. Due to higher mass, the velocity of ERs is lower than the velocity of projectiles, which allows setting a specific E/B ratio allowing only ERs to pass through the separator.

After the second electric deflector, another quadrupole triplet is placed to focus separated reaction products. One dipole magnet is further downstream to provide an additional 7.5° deflection to separate reaction products from high-energy background passing through the separator.

The SHIP accepts ions with a relative velocity width of $\pm 5\%$ and a charge state width of $\pm 10\%$. Flight time of the ERs through the SHIP is around $2\mu\text{s}$. Total background suppression can reach the factor of $10^7 - 10^{11}$. The total transmission coefficient (ratio between the number of ERs entering the filter and the number of ERs leaving the filter) of the reaction products is heavily dependent on the mass (a)symmetry of the projectile and target nuclei. More symmetric reactions (e.g. $^{136}\text{Xe} + ^{136}\text{Xe}$) can reach up to 100% transmission, while very asymmetric reactions like $^{12}\text{C} + ^{194}\text{Pt}$ reach only around 2%, see Fig. 2.2 and ref. [Maz08]. After the separation, reaction products are implanted into the focal plane of the detector system.

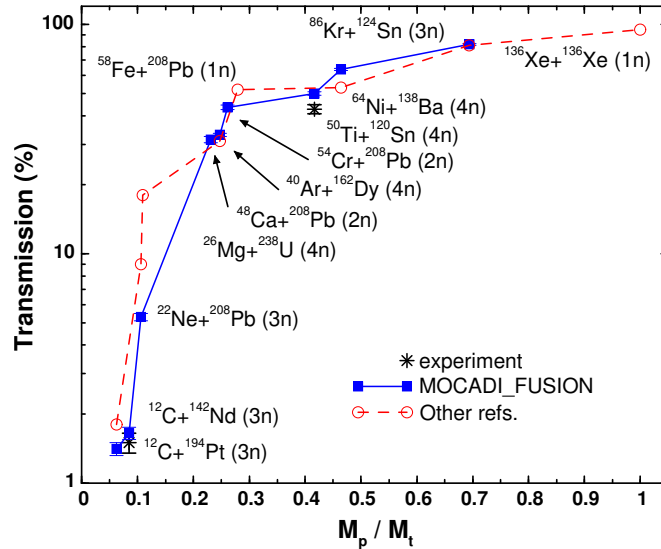


Figure 2.2: SHIP transmission - comparison of the experimental (black asterisks) and theoretical values calculated by the code MOCADI_FUSION (blue line). The red line represents values from [Pop97; Pop99]. Figure taken from [Maz08].

2.3 Detector system

After the separation, reaction products fly through the time-of-flight (TOF) system and are implanted into the detector system at the focal plane of the beam (Fig. 2.3).

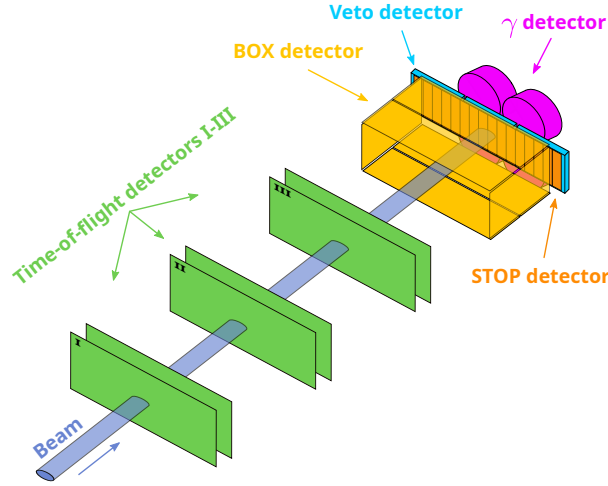


Figure 2.3: Detector setup behind the SHIP (not to scale).

The detector system consists of two or three TOF detectors, seven position-sensitive silicon strip detectors (PSSD) - one implantation PSSD (STOP) and six PSSDs in the backward direction (BOX), veto detector, and germanium clover array.

TOF system

TOF system consists of two or three (depending on the experiment) TOF detectors 15 mm apart [Šár96]. Each TOF detector is made up of two self-supporting $30 \mu\text{g}/\text{cm}^2$ thick carbon foils, with 55 mm^2 active area. After a reaction product passes a foil, electrons are emitted. An electric potential of 4 kV is applied between the foils to accelerate emitted electrons, while a perpendicular magnetic field bends electrons onto microchannel plates for amplification and signal reading. The transparency of the TOF system is 100% and the time resolution is 700 ps. The efficiency is around 99.8% for two and close to 100% for three TOF detectors. The TOF system used in anticoincidence with the STOP detector allows us to distinguish between signals induced by particles/nuclei coming from the separator and the signals induced by the decays of already implanted nuclei. From the time resolution of the TOF system and energy detected in the STOP detector, rough mass determination with an accuracy of $\pm 10\%$ is achievable [Hof00].

PSSD - STOP and BOX detectors

A PSSD consists of 16 silicon strips with a total active area of $35 \times 80 \text{ mm}^2$. Each strip is 35 mm long, 5 mm wide and $300 \mu\text{m}$. Vertical position resolution is $\sim 150 \mu\text{m}$ ¹ for an α decay. Due to the position sensitivity, one PSSD is equivalent to 3700 single detectors, each with $0.15 \times 5 \text{ mm}^2$ active area. A typical energy resolution is 14 keV for ^{241}Am as an external source [Hof00]. All PSSDs are cooled down to 263 K.

In reality, a sum of an α -particle energy and the kinetic energy of the recoiling nucleus after an α decay is detected. Due to the pulse height defect (PHD) affecting the detection of the recoiling nucleus, position resolution is worse - around 0.5 mm. The energy resolution is also affected by the PHD, summing of the spectra from individual strips and non-ideal calibration and is at around 20 keV,

One PSSD is placed in the focal plane of the beam coming from the separator. Here, ERs are implanted and stopped, hence the name STOP detector. Due to the range of α particles (and fission fragments (FF)) in silicon being significantly larger than the range of ERs, α particles/FFs can escape the STOP detector in the backward direction without depositing full energy. This situation is displayed in Fig. 2.4.

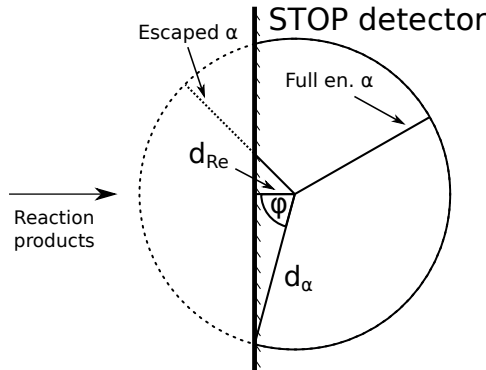


Figure 2.4: Geometric efficiency for detection of full energy α particles after implantation into the STOP detector.

The ratio between an angle φ and full 180° (π) angle determines part of the α particles *escaped* from the STOP detector. Therefore, the geometric efficiency for fully registering an α particle is:

$$\varepsilon_{geom} = 1 - \frac{\varphi}{180^\circ} = 1 - \frac{\arccos \frac{d_{Re}}{d_\alpha}}{180^\circ} \quad (2.1)$$

For example, in $^{46}\text{Ti}+^{144}\text{Sm}$ reaction at 239.2 MeV beam energy, evaporation residue ^{186}Bi is implanted into the STOP detector with an energy of $\sim 20 \text{ MeV}$ (after energy lost in the target, TOF system, mylar degraders etc.) and decays via α decay with $E_\alpha = 7.2 \text{ MeV}$. The corresponding implantation depths are $d_{Re} \approx 3.6 \mu\text{m}$ and $d_\alpha \approx 41 \mu\text{m}$.

¹All resolutions are noted as FWHM

From eq. 2.1, geometric efficiency of detecting full energy α particles is around 52.8%. Energy losses and implantation depths were calculated with LISE++ [Tar08].

To increase the geometric efficiency of the STOP detector, another six PSSDs are placed upstream of the beam in a box-like shape (hence the name BOX or BACK detectors). Neighboring strips of BOX detectors are connected galvanically, creating 28 segments. The geometric efficiency of the BOX detectors reaches 80% of 2π half-space in front of the STOP detector and the energy resolution of the STOP+BOX system is around 70 keV. This decrease in resolution (compared to ~ 20 keV of STOP detector) is because particles/FFs have to pass through dead layers of both STOP and BOX detectors, which is around $10 \mu\text{g}/\text{cm}^2$ thick. Coincidences between STOP and BOX detectors allow us to reconstruct the full energy of the α particles/FFs.

In front of the silicon detector array, degrader foils, usually from Mylar, can be installed. The thickness of foils can be adjusted in increments of $0.5 \mu\text{m}$ up to several μm . Degraded foils are used to absorb low-energy projectiles passing through SHIP and to reduce the implantation depth of ERs (to eliminate low-energy "tails" from escaped particles). The ability to adjust implantation depth is crucial especially for the total kinetic energy determination of FFs, since the effect of the pulse-height defect varies with the implantation depth of ERs [Mos20].

Veto detector

A veto silicon detector is placed behind the STOP detector. Its purpose is to detect particles - usually high-energy protons - that pass through the STOP detector and are not registered by the TOF system. These signals are then rejected based on the coincidences between STOP-Veto detectors. Similarly to PSSDs, the Veto detector is cooled down to 263 K.

Germanium clover detector

Closely behind the array of silicon detectors, a germanium detector for the detection of X-rays and γ quanta is placed. In the past experiments, only one single germanium crystal was used, which did not allow measurement of the $\gamma-\gamma$ coincidences. Nowadays, a system of four identical germanium crystals arranged in a clover-like shape is used, hence the name clover detector. Two clovers with different volumes are usually used:

- VEGA type clover detector [Kas98]: four crystals with a diameter of 70 mm each and shaped and formed into a block with dimensions $(124 \times 124 \times 140) \text{ mm}^3$.
- SHIP clover detector [Heß10]: four crystals with a diameter of $(50-55) \text{ mm}$ each and shaped and formed into a block with dimensions $(102 \times 102 \times 70) \text{ mm}^3$.

VEGA clover provides better efficiency for detecting high-energy quanta, compared to the SHIP clover. The energy resolution of the germanium detectors is around (1.4-2.1) keV. Due to relatively low detection efficiency of around (10-12)% for 130 keV γ quanta, $\gamma - \gamma$ coincident measurements require relatively high statistics.

2.4 Data analysis

2.4.1 Electronics and signal processing

In an experiment, signals from different sources (particles, projectiles, transfer products, ERs, FFs, γ quanta, ...) with a wide variety of energies from a few keV to hundreds of MeV are registered, and processed.

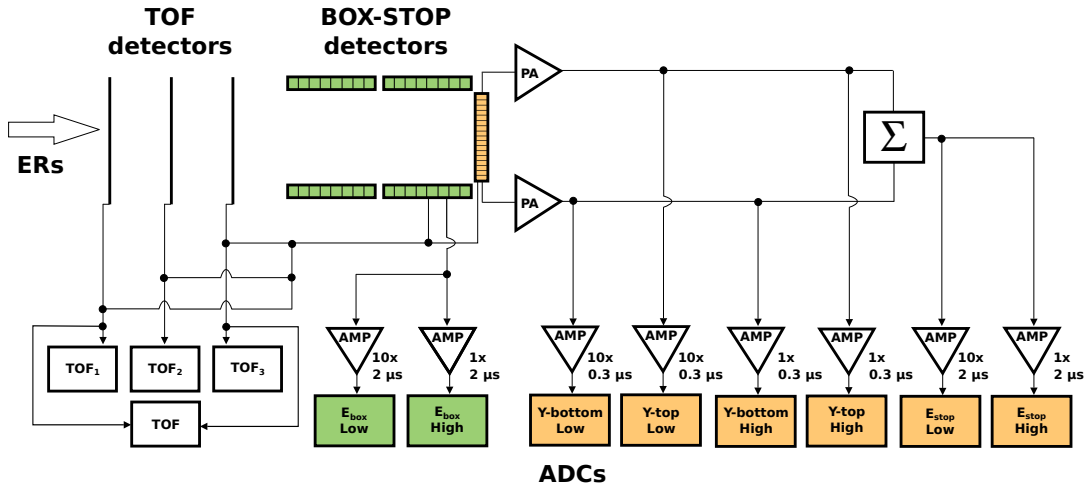


Figure 2.5: Schematic representation of the electronic system of STOP, BOX, and TOF detectors. Figure adapted from [Štr06].

The electronic system (Fig. 2.5) is divided into two branches, separate for low- and high-energy signals:

- Low-energy branch: processes signals up to ~ 16 MeV from the STOP and BOX detectors and up to ~ 1500 keV from germanium detectors with an amplification factor of 10.
- High-energy branch: processes signals from ~ 4 –300 MeV from the STOP and BOX detectors and up to ~ 8 MeV from germanium detectors without an amplification.

Signals from the detector are processed with fast analog-to-digital converters with 3.5- μ s conversion time and 128-word first-in-first-out (FIFO) buffers in each channel [Hof00]. The signal width is determined by the shaping time constants, 0.3 μ s is used for the position and 2 μ s for the energy signals.

Time differences $\Delta t(\text{particle} - \gamma)$ between particle- γ signals are handled based on the time intervals [Ant11]:

- Time differences $\Delta t(\text{particle} - \gamma) < 5 \mu\text{s}$ are determined by the coincidence time of the data acquisition system and are measured with time-to-amplitude converters (TAC) with a resolution of 200 ns.
- Time differences $\Delta t(\text{particle} - \gamma) > 25 \mu\text{s}$ are measured by a continuously running clock with a resolution of 1 μs .

Time interval $\Delta t(\text{particle} - \gamma) = (5-25) \mu\text{s}$ is inaccessible due to the dead time of the data acquisition system.

In [Ant11], the time of the prompt coincidences was delayed by $\approx 0.8 \mu\text{s}$ and in the analysis $\text{TAC}_{\text{prompt}} = 0 \mu\text{s}$ was set. Therefore, coincidences of γ quanta emitted *before* the particles were measured as well (with $\text{TAC} < 0 \mu\text{s}$). Coincidences with $\text{TAC} > 0 \mu\text{s}$ were due to γ quanta emitted *after* the particles within $\approx 2.6 \mu\text{s}$.

To determine the vertical position along the strip in the STOP detector, a signal is taken from the top and bottom of the strip separately. The total energy is then the sum of the top and bottom signals. Position determination along the strip is done by comparing the energy signal from the top and bottom of the strip to the total energy. The BOX detector is not position-sensitive, due to the galvanic connections between the strips.

The analysis of experimental data is performed with the use of Object-Oriented On-line Off-line system (Go4) [Ada08]. Go4 is based on the object-oriented analysis system ROOT [Bru97], with implemented extensions required for medium and low nuclear and atomic physics experiments.

2.4.2 Time-position correlation technique

This powerful technique was first introduced in 1979 and used in alpha decay studies of neutron deficient isotopes [Hof79]. It is based on the fact that implantation and any subsequent α /SF decays of ER and its daughter nuclei have the same vertical position when compared to its resolution. The principle is shown in Fig. 2.6.

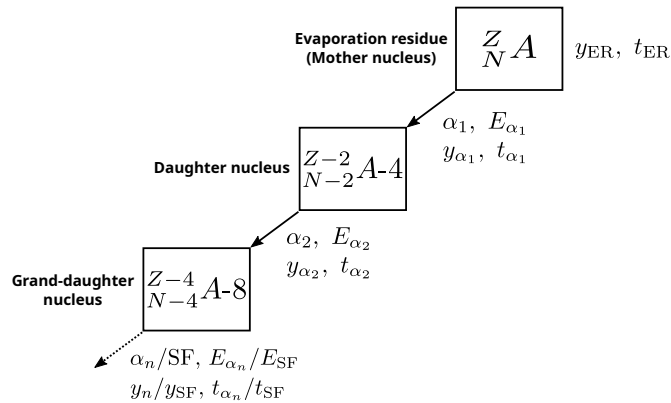


Figure 2.6: Correlation technique principle.

By adjusting correlation conditions, the technique enables us to study nuclei one-by-one and provides significant background suppression (comparison is in Fig. 2.7). Time window of around 3–5 times of $T_{1/2}$ of the corresponding nucleus and position window of 0.8 mm for α – α and ER– α were used throughout the work. The position window size is based on the correlation search focused on a short-lived isotopes (in order to eliminate random correlations) and the corresponding position-difference distributions. Correlation technique enables the half-life determination of the studied nuclei and separation of the overlapping α decay energies if they have different half-lives. New isotopes can be identified by reconstructing the decay chain from the decays of known daughter nuclei back to unknown mother nucleus. Special case is the correlation search of conversion electrons, when the energy losses of electrons are not high enough to produce a position signal in the strip detector - therefore no position condition is used.

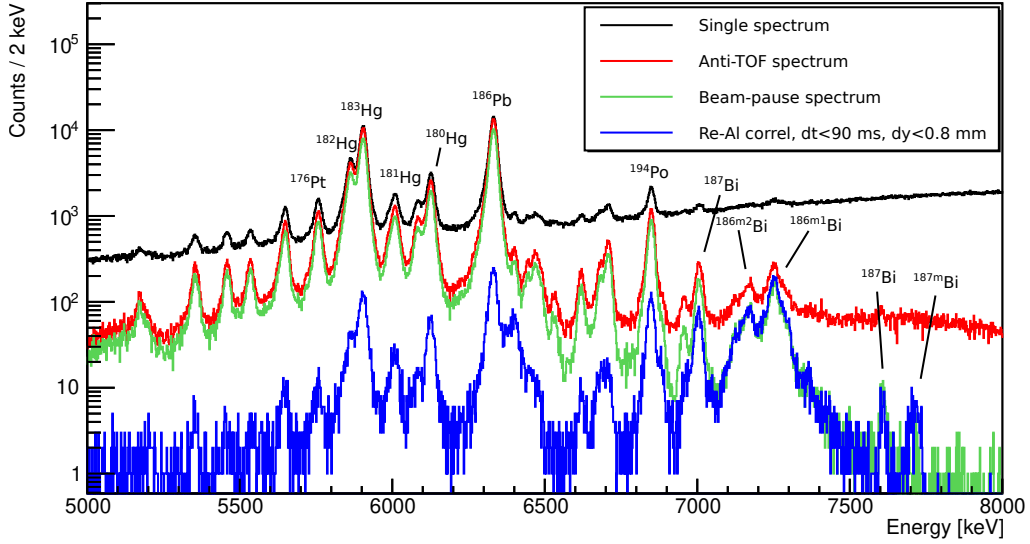


Figure 2.7: Background suppression of different methods. Black line represents all events in the STOP detector, red line are events in anti-coincidence with TOF system, green line are events from the beam-pause and blue line are events from the ER- α correlation search within 90 ms time window and 0.8 mm position window.

The effect of the correlation method can be demonstrated on $^{186,187}\text{Bi}$ isotopes and isomers in Fig. 2.7. These nuclei have rather short half-lives (0.37 ms of ^{187m}Bi , 37 ms of ^{187}Bi , $\sim(10-15)$ ms of $^{186m1,m2}\text{Bi}$) and therefore the correlation search (with the time window of 90 ms) does not significantly decrease their numbers in comparison to the anti-TOF and beam-pause spectra. In contrast, numbers of events from the isotopes with high half-lives, such as ^{186}Pb (4.82 s), ^{194}Po (0.392 s) and ^{183}Hg (9.4 s), are decreased by around 2 orders, but are still present mainly as random correlations.

2.4.3 Statistical analysis in case of poor statistics

Amount of the studied events is often not sufficient to use the statistical analysis. K.-H. Schmidt in [Sch84a] presented several relations which allow to calculate the significance of correlated chains and estimate uncertainties of number of events and half-lives, even in case of single events.

Random correlations evaluation

In case of high half-lives of the correlated nuclei, large time window conditions must be used and random correlations start to appear. The amount of random correlations n_r can be estimated as in [Sch84a]:

$$n_r = T\lambda_1 \dots \lambda_i \Delta t_{1,2} \dots \Delta t_{i,i+1} \quad (2.2)$$

where T is the total measure time, i is the total number of correlation groups, λ_i is the counting rate (events per second) of the corresponding group and $\Delta t_{i,i+1}$ is the corresponding correlation time window between i and $i+1$ group. The counting rate also reflects the correlation position window.

Error determination for small numbers

Countrate uncertainties - Poisson distribution The probability to observe n events while μ is the mean value of the number of events is described by the Poisson distribution:

$$p(n|\mu) = \frac{\mu^n}{n!} e^{-\mu} \quad (2.3)$$

For the confidence level $(1 - \varepsilon)$ (ε is an error probability) and a number of observed events n_m , the confidence lower (μ_l) and upper (μ_u) limits are given as the solutions of the following equations:

$$\begin{aligned} \sum_{n=n_m}^{\infty} p(n|\mu_l) &= 1 - \sum_{n=0}^{n_m-1} \frac{\mu_l^n}{n!} e^{-\mu_l} = \frac{\varepsilon}{2} \\ \sum_{n=0}^{n_m} p(n|\mu_u) &= \sum_{n=0}^{n_m} \frac{\mu_u^n}{n!} e^{-\mu_u} = \frac{\varepsilon}{2} \end{aligned} \quad (2.4)$$

An accurate approximation of the lower and upper confidence limits for small numbers and $n_m \geq 2$ is

$$\begin{aligned}\mu_l &\approx n_m - z\sqrt{n_m} \\ \mu_u &\approx n_m + z(1 + \sqrt{n_m})\end{aligned}\tag{2.5}$$

Parameter z is related to the chosen confidence level $(1 - \varepsilon)$ through

$$\frac{\varepsilon}{2} = \int_z^\infty \frac{1}{\sqrt{2\pi}} e^{-x^2/2} dx\tag{2.6}$$

and for the standard error $z = 1$ (confidence level $(1 - \varepsilon) = 0.68$). This approximation for small numbers is much more accurate than the conventionally used symmetric errors

$$n_m - \mu_l = \mu_u - n_m = z\sqrt{n_m}\tag{2.7}$$

Comparison of the exact confidence limits given by the equation 2.4, the approximation by the equation 2.5 and the symmetric errors (eq. 2.7) is in Fig. 2.8a. Standard errors for $n_m \leq 2$ are summarized in the table 2.1.

Lifetime uncertainties - exponential distribution The arithmetic mean $\overline{t_m}$ of the lifetimes $(t_m)_i$ at which the events were observed gives the maximum likelihood estimate of the lifetime τ :

$$\overline{t_m} = \frac{1}{n} \sum_{i=1}^n (t_m)_i\tag{2.8}$$

The confidence lower (τ_l) and upper (τ_u) limits of the lifetime determination of n observed events can be expressed as the solution of the following equations

$$\begin{aligned}\int_{\overline{t_m}}^\infty p_n(t|\tau_l) d\bar{t} &= \sum_{n=0}^{n-1} \left(\frac{n\overline{t_m}}{\tau_u} \right)^n \frac{1}{n!} e^{-n\overline{t_m}/\tau_l} = \frac{\varepsilon}{2} \\ \int_0^{\overline{t_m}} p_n(t|\tau_u) d\bar{t} &= 1 - \sum_{n=0}^{n-1} \left(\frac{n\overline{t_m}}{\tau_u} \right)^n \frac{1}{n!} e^{-n\overline{t_m}/\tau_u} = \frac{\varepsilon}{2}\end{aligned}\tag{2.9}$$

where $\overline{t_m}$ is the observed value for \bar{t} and \bar{t} is the mean observed value. An accurate approximation for these confidence limits for small numbers and $n \geq 2$ is

$$\begin{aligned}\tau_l &\approx \frac{\overline{t_m}}{1 + z/\sqrt{n}} \\ \tau_u &\approx \frac{\overline{t_m}}{1 - z/\sqrt{n}}\end{aligned}\tag{2.10}$$

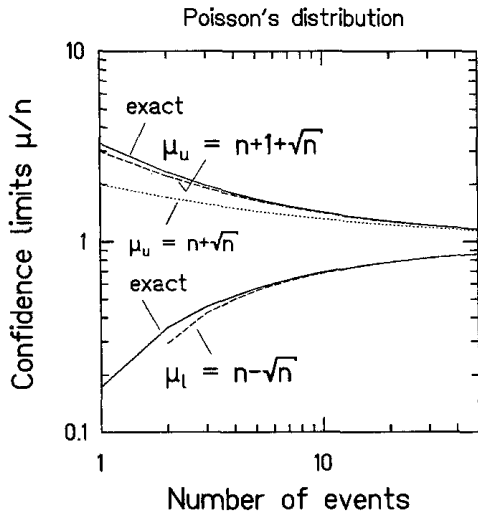
Parameter z is expressed by the equation 2.6. This approximation is much more accurate than the conventionally used symmetric errors

$$\overline{t_m} - \tau_l = \tau_u - \overline{t_m} = z \frac{\overline{t_m}}{\sqrt{n}} \quad (2.11)$$

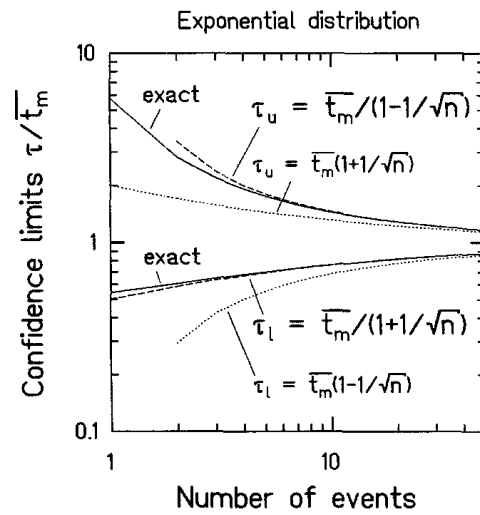
Comparison of the exact confidence limits given by the equation 2.9, the approximation by the equation 2.10 and the symmetric errors (eq. 2.11) is in Fig. 2.8b. Standard errors (confidence level $(1 - \varepsilon) = 0.68$) for $n_m \leq 2$ are summarized in the table 2.1.

Table 2.1: Standard errors (confidence level $(1 - \varepsilon) = 0.68$) for number of observed events $n \leq 2$, calculated from the equations 2.4 (Countrate column) and 2.9 (Lifetime column). Cases where the approximations by the equations 2.5 and 2.10 are within 10% from the exact values are given in parentheses.

Number of observed counts n	Countrate		Lifetime	
	μ_l	μ_u	$\tau_l/\overline{t_m}$	$\tau_u/\overline{t_m}$
0	0	1.84	-	-
1	0.173	(3.3)	(0.543)	5.79
2	(0.708)	(4.64)	(0.606)	(2.82)



(a) The confidence limits of the events following the Poisson distribution.



(b) The confidence limits of the events following the exponential distribution.

Figure 2.8: Confidence limits for a confidence level $(1 - \varepsilon) = 0.68$ ($z = 1$) as the functions of observed events. Solid lines denote exact values derived from the equations 2.4 and 2.9, dashed lines are approximations from the equations 2.5 and 2.10, in figs. 2.8a and 2.8b, respectively. Dotted lines denote conventional symmetric errors. Figure reprinted from [Sch84a].

Chapter 3

Objectives of the project

In this chapter main aims of the dissertation project will be presented. The project will be divided into two parts:

- decay spectroscopy of ^{186}Bi and its α decay product ^{182}Tl
- study of cross sections systematics in the reactions leading to compound nuclei from the radon–radium region

For each part, the previous studies of the topic are summarized.

3.1 Decay spectroscopy of ^{186}Bi

The main aim is to analyze the structure of ^{182}Tl , produced as an α decay product of ^{186}Bi , via $\alpha - \gamma$ coincidence analysis. Currently, data from the reactions $^{46}\text{Ti}+^{144}\text{Sm}$ and $^{95}\text{Mo}+^{93}\text{Nb}$ (already analyzed in [And03]) measured at the SHIP are available, the merger of the datasets increased the total number of ^{186}Bi collected almost three times in comparison with the analysis in the reference. The statistics increase allows to assign the majority of γ signals in coincidences with α decays originating from either isomer in ^{186}Bi .

More specifically, the completion of the following goals is expected:

- Calibration of the detector setup: calibration of PSSD with a use of known α peaks; calibration of the γ detector with a use of ^{152}Eu ; determination of the efficiency curve of the γ detector.
- Identification of the produced nuclei.
- Determination of the half-lives of both ^{186}Bi isomers, to verify the previously determined value from [Bat97; And03].

- Analysis of the $\alpha - \gamma$ coincident spectra, with an emphasis on the γ lines coincident with the α decay of ^{186}Bi . The $Q(\alpha) + E_\gamma$ value for each $\alpha - \gamma$ group will be determined, along with the corresponding half-lives extracted from the $ER - (\alpha - \gamma)$ correlation search.
- In case of the complex α distributions of $\alpha - \gamma$ groups, which will indicate $\alpha + \text{CE}$ summing effects, the tentative determination of the converted transitions - their energy and multipolarity - will be performed.
- The decay scheme of ^{186}Bi and of the states in ^{182}Tl will be constructed.

3.1.1 Previous studies of ^{186}Bi

Alpha decay activity of ^{186}Bi was first observed by J. R. H. Schneider [Sch84b]. He reported one 7191(25) keV α activity with a half-life of 10(4) ms.

Further study conducted by J. C. Batchelder [Bat97] examined ^{186}Bi produced in a $^{97}\text{Mo}(^{92}\text{Mo}, p2n)$ reaction. Two α activities correlated with α particles from the α decay of ^{182}Hg (produced by β^+/EC of ^{186}Bi α -decay daughter product, ^{182}Tl) were observed - 7158(20) keV with $T_{1/2} = 15.0(17)$ ms a 7261(20) keV with $T_{1/2} = 9.8(13)$ ms. Higher energy (shorter-lived) activity was assigned to (10^-) and lower energy (longer-lived) activity was assigned to (3^+) isomeric state in ^{186}Bi , based on the systematics from [Van91] aimed on the investigation of heavier odd-odd bismuth isotopes ($^{190-196}\text{Bi}$) and due to higher intensity of 7261 keV α line (since higher spin states are expected to be populated preferentially).

The later study [And03] investigated ^{186}Bi produced in the $^{95}\text{Mo}(^{93}\text{Nb}, 2n)^{186}\text{Bi}$ complete fusion reaction measured at the SHIP, GSI at 419 and 438 MeV beam energies in front of the target. The collected statistics was around 50 times greater than in the previous studies, which allowed the measurement of coincident γ rays after α decay of ^{186}Bi and provided more detailed information about the nuclide. The study reported two α activities (similarly to [Bat97]), with 7261(20) keV and 7152(15) keV energies and 9.8(4) ms and 14.8(8) ms half-lives, denoted as $^{186m1}\text{Bi}$ and $^{186m2}\text{Bi}$, respectively¹. Based on the $\alpha - \gamma$ coincidence analysis and $Q(\alpha) + E_\gamma$ summing, 7080-520 and 7152-444 keV $\alpha - \gamma$ groups were assigned to the $^{186m2}\text{Bi}$ isomer and 7263-108.5 keV was assigned to the $^{186m1}\text{Bi}$. The most intense, 108.5 keV γ transition was assigned $E1$ multipolarity based on the GEANT4 Monte Carlo simulations. Other $\alpha - \gamma$ groups were not assigned due to low statistics, $\alpha - e^-$ summing effects emerging from the internal conversion and similar half-lives of both isomers. Direct, full energy crossovers of either isomer were not observed or could not be resolved.

¹This notation will be used throughout the work.

3.2 Cross section studies

Data from the $^{52}\text{Cr}+^{147,149,150}\text{Sm} \rightarrow ^{199,201,202}\text{Rn}^*$ and $^{56}\text{Fe}+^{147,149,154}\text{Sm} \rightarrow ^{203,205,210}\text{Ra}^*$ reactions measured at the SHIP are available. Main aim is to obtain experimental cross sections of the reaction products for different reactions and compare them with the theoretical calculations according to the statistical code HIVAP (section 1.1.1). By optimizing the theoretical predictions to reproduce the experimental values, an optimal fission barrier scaling parameter will be extracted.

More specifically, the completion of the following goals is expected:

- Calibration of the detector setup for each reaction: calibration of PSSD with a use of known α peaks; calibration of the γ detector with a use of ^{152}Eu ; determination of the efficiency curve of the γ detector.
- Identification of the produced isotopes based on known α energies and half-lives. The differentiation between the isotopes with similar α decay energies will be based on the $\alpha - \gamma$ coincidence analysis. Alternatively, the use of the correlation technique can be employed, however, relatively long half-lives of the expected reaction products could be a limiting factor.
- Evaluation of the experimental cross sections and of the corresponding statistical uncertainties.
- Theoretical calculations of the excitation functions via the code HIVAP - the variation of the fission barrier scaling parameter will allow to fit the experimental values. The decrease of the parameter in the compound nucleus ^{202}Rn by around 27% is expected (according to the systematics from [And05]). Additionally, the theoretical cross sections can be evaluated by alternative approaches and models, such as Nuclear Reaction Video (NRV) calculation [Kar17] or the evaluation by the software LISE++ [Tar08], and compared with the HIVAP.
- Extraction of the optimal scaling parameter value for each of the analysed reaction will allow to extend known systematics by radon and radium compound nuclei.

3.2.1 Previous studies of the cross section systematics in the lead region

The production of the neutron-deficient polonium and bismuth isotopes was studied by using FERs measured at the SHIP, GSI. The cross sections of the xn and pxn evaporation channels in the reactions $^{46}\text{Ti}+^{144}\text{Sm} \rightarrow ^{190}\text{Po}^*$, $^{98}\text{Mo}+^{92}\text{Mo} \rightarrow ^{190}\text{Po}^*$, $^{50,52}\text{Cr}+^{142}\text{Nd} \rightarrow ^{192,194}\text{Po}^*$ and $^{94,95}\text{Mo}+^{93}\text{Nb} \rightarrow ^{187,188}\text{Bi}^*$ were evaluated. The experimental results together with known cross section data for the other heavier polonium and bismuth isotopes were

compared with the theoretical calculations obtained from the statistical model HIVAP (section 1.1.1) [And05].

The parameters entering the theoretical calculations had fixed values corresponding to the studied reaction. The only free parameter of the calculation was the scaling factor of the liquid-drop model fission barrier. To reproduce the experimental data with the theoretical calculations, the decrease of the fission barrier by a factor of up to 35% was required. The difference between the theoretical cross sections calculated with such scaled barrier and unscaled one can reach up to three orders of magnitude.

Chapter 4

Preliminary results

4.1 Investigation of ^{186}Bi

4.1.1 Experimental details

Two reactions producing the isotope ^{186}Bi were measured at the SHIP, GSI. The reaction $^{95}\text{Mo}(^{93}\text{Nb}, 2n)^{186}\text{Bi}$ already mentioned in section 3.1.1, was measured during the experiment R206 at 419 and 438 MeV beam energies and α decay spectroscopic results about ^{186}Bi were published in [And03]. Target made of metallic ^{93}Nb with thickness of $900\text{ }\mu\text{g}/\text{cm}^2$ was irradiated by ^{95}Mo beam with an intensity of about 10 pA. Beam energies of 419 and 438 MeV in front of the target correspond to the excitation energies of about 31.3 and 40.7 MeV in the middle of the target, respectively.

The other studied reaction was $^{46}\text{Ti}(^{144}\text{Sm}, p3n)^{186}\text{Bi}$ measured during the experiment R224 at beam energies ranging from 207 to 247 MeV. The target was $400\text{ }\mu\text{g}/\text{cm}^2$ thick composed of $^{144}\text{SmF}_3$, corresponding to about $287\text{ }\mu\text{g}/\text{cm}^2$ of pure ^{144}Sm . The highest yield of ^{186}Bi was obtained at the beam energy of 239.2 MeV, which corresponds to the excitation energy of about 57.6 MeV in the middle of the target (energy losses were calculated with software LISE++ [Tar08]).

4.1.2 Alpha–gamma coincidence approach

The amount of ^{186}Bi α decays of (in the range of 7050–7500 keV) collected between beam pulses is about 4500 and 9000 in $^{95}\text{Mo}+^{93}\text{Nb}$ and $^{46}\text{Ti}+^{144}\text{Sm}$ reactions, respectively. The combination of data therefore triples the statistics used in the previous study [And03]. The spectra of single α decays (recorded between beam pulses) and of α decays correlated with ER within 90 ms (about five times the half-life of $^{186m2}\text{Bi}$ - 14.8 ms) and 0.8 mm position window are shown in Fig. 4.1. In the correlation search, also α signals collected during the beam pulses were selected, since the restrictive conditions significantly suppress α decays of other, longer-lived isotopes.

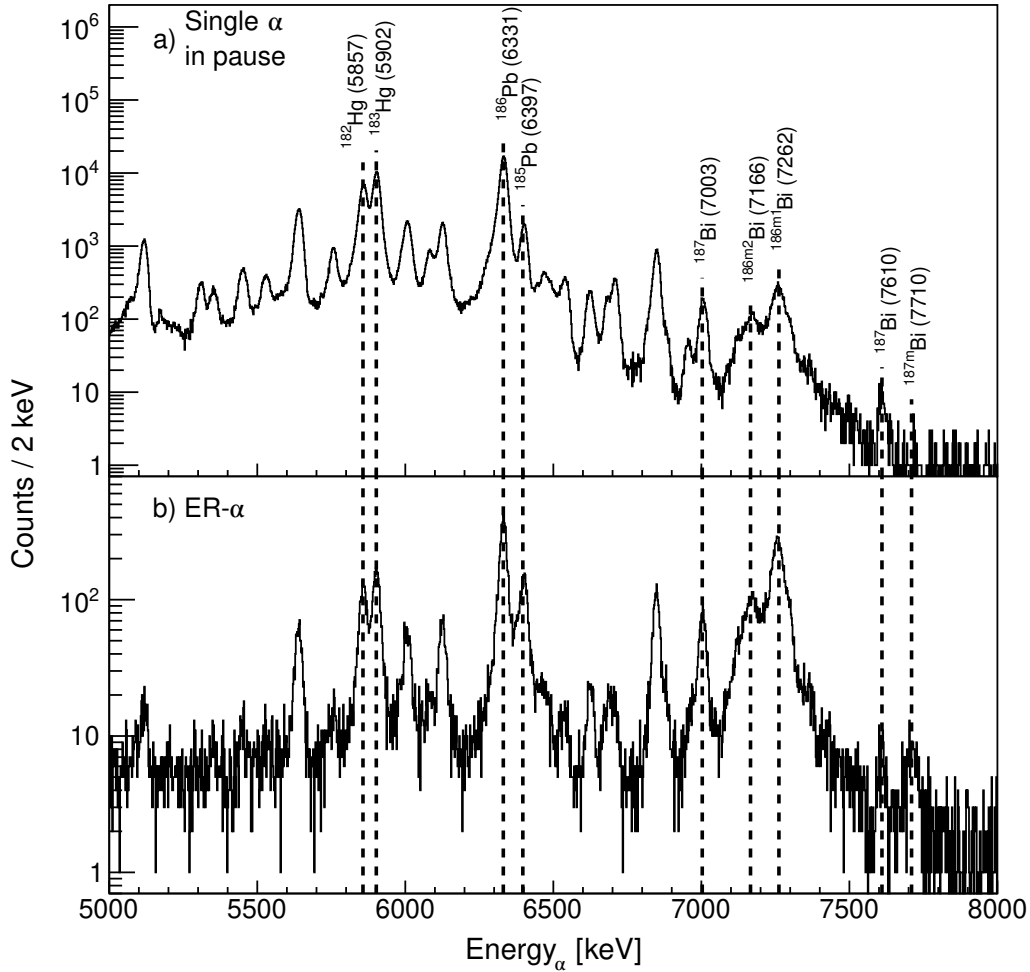


Figure 4.1: Alpha-decay energy spectra combined from $^{95}\text{Mo}+^{93}\text{Nb}$ (at 419 and 438 MeV beam energies) and $^{46}\text{Ti}+^{144}\text{Sm}$ (at 239.2 MeV beam energy) reactions: a) α particles detected between beam pulses; b) α particles (with anti-TOF condition) from ER- α correlations registered within 90 ms of the implantation of the ER with a position difference of ≤ 0.8 mm.

Isotope ^{182}Hg is the daughter product of $^{186m1,m2}\text{Bi}$ originating in the decay sequence $^{186}\text{Bi} \xrightarrow{\alpha} ^{182}\text{Tl} \xrightarrow{\beta} ^{182}\text{Hg}$. Along with the production of ^{186}Bi in $^{95}\text{Mo}(^{93}\text{Nb}, 2n)^{186}\text{Bi}$ and $^{46}\text{Ti}(^{144}\text{Sm}, p3n)^{186}\text{Bi}$ reactions, other identified isotopes are most likely produced directly through $^{95}\text{Mo}(^{93}\text{Nb}, \alpha n)^{183}\text{Hg}$, $^{95}\text{Mo}(^{93}\text{Nb}, pn)^{186}\text{Pb}$, $^{46}\text{Ti}(^{144}\text{Sm}, 2p2n)^{186}\text{Pb}$, $^{46}\text{Ti}(^{144}\text{Sm}, \alpha n)^{185}\text{Pb}$ and $^{46}\text{Ti}(^{144}\text{Sm}, p2n)^{187}\text{Bi}$ reactions.

The half-life determination of either isomer was performed with the use of ER- α correlations separately for each reaction. Obtained decay curves were fitted using maximum likelihood minimizing method. The α particles were chosen from energy intervals $E_\alpha = 7121 - 7196$ keV for $^{186m2}\text{Bi}$ and $E_\alpha = 7223 - 7298$ keV for $^{186m1}\text{Bi}$, to eliminate overlapping of the two isomers. The requirement in the correlation search was the time difference $\Delta T(\text{ER} - \alpha) \leq 90$ ms, position window of 0.8 mm and α decays registered also during beam pulses were taken into account. Further, to confirm the half-life of $^{186m1}\text{Bi}$, an additional requirement was coincident γ signal with α signal with an energy of $E_\gamma = 106 - 108$ keV which is the most intense transition in $^{186m1}\text{Bi}$. The results are

summarized in table 4.1.

Table 4.1: Half-lives extracted from the ER- α correlation search. Gates on the alpha-decay energies (denoted in brackets) were chosen to obtain the $\Delta T(\text{ER} - \alpha)$ distributions of either isomer. Additionally, in the last row γ signal with energy $E_\gamma = 106 - 110$ keV was required. For each reaction, half-lives were determined separately and also from the combined data. Obtained values are compared with the values from the previous study [And03].

Data	$T_{1/2}$ [ms]			
	$^{46}\text{Ti}+^{144}\text{Sm}$ (R224)	$^{95}\text{Mo}+^{93}\text{Nb}$ (R206)	Combined R224+R206	Ref. [And03]
$^{186m2}\text{Bi}$ ($E_\alpha = 7121 - 7196$ keV)	9.4(5)	14.8(19)	9.9(4)	14.8(8)
$^{186m1}\text{Bi}$ ($E_\alpha = 7223 - 7298$ keV)	7.2(3)	8.6(5)	7.8(2)	9.8(4)
$^{186m1}\text{Bi}$ ($E_\alpha = 7223 - 7298$ keV "AND" $E_\gamma = 106 - 110$ keV)	7.2(7)	8.4(10)	7.7(6)	-

The half-life values of both isomers determined from the reaction $^{95}\text{Mo}+^{93}\text{Nb}$ are within the error margin from the values reported in [And03] and [Bat97]. The values determined from the $^{46}\text{Ti}+^{144}\text{Sm}$ reaction are significantly different, especially the half-life of $^{186m2}\text{Bi}$. Additional requirement of γ signal with $E_\gamma = 108 \pm 2$ keV coincident with correlated α decay confirmed the half-life of $^{186m1}\text{Bi}$, without a possible admixture of α signals from $^{186m2}\text{Bi}$. However, such procedure requires a sufficient amount of the corresponding γ signals, which was not the case in the transitions originating from the $^{186m2}\text{Bi}$. A discrepancy between $^{186m2}\text{Bi}$ half-lives could be caused by a stronger overlapping of $m1$ and $m2$ alpha decay energies emerging from a different population of high-spin ($^{186m1}\text{Bi}$) and low-spin ($^{186m2}\text{Bi}$) isomers in symmetric reactions (studied in [And03; Bat97]) and more asymmetric $^{46}\text{Ti}+^{144}\text{Sm}$ reaction studied in this work.

Two-dimensional spectrum of $\alpha - \gamma$ coincidences measured within $\Delta T(\alpha - \gamma) \leq 5$ ms with the α decays from the interval 7050 – 7500 keV (those of $^{186m1,m2}\text{Bi}$) is in the top panel of Fig. 4.2. Corresponding projection into the E_γ axis is in the bottom panel of Fig. 4.2. Coloured lines represent $Q(\alpha) + E_\gamma = Q$ values of either isomer.

Several γ lines can be clearly distinguished from the projection of γ energies (bottom panel in Fig. 4.2). The most intense lines at 72.5 and 83.5 keV are K_α and K_β X rays of thallium (see table 1.2), which is produced as the α decay product of ^{186}Bi .

Based solely on the sum of $Q(\alpha) + E_\gamma$, γ lines with the energies of 97, 108 and 169 keV could be attributed to the de-excitation following the α decay of $^{186m1}\text{Bi}$ isomer. Similarly, lines with the energies of 371, 426, 445 and 520 keV were attributed to the transitions following the decay of $^{186m2}\text{Bi}$. Other γ lines with the energies of 186, 215, 238, 248 and 255 keV could be assigned to the $^{186m1}\text{Bi}$ isomer as well, however the determination of the corresponding α energies (and thus the Q values) was very ambiguous and inconclusive. The summary of γ transitions and corresponding α energies from the $\alpha - \gamma$ coincidence analysis is in the table 4.2 and the resulting, preliminary decay scheme

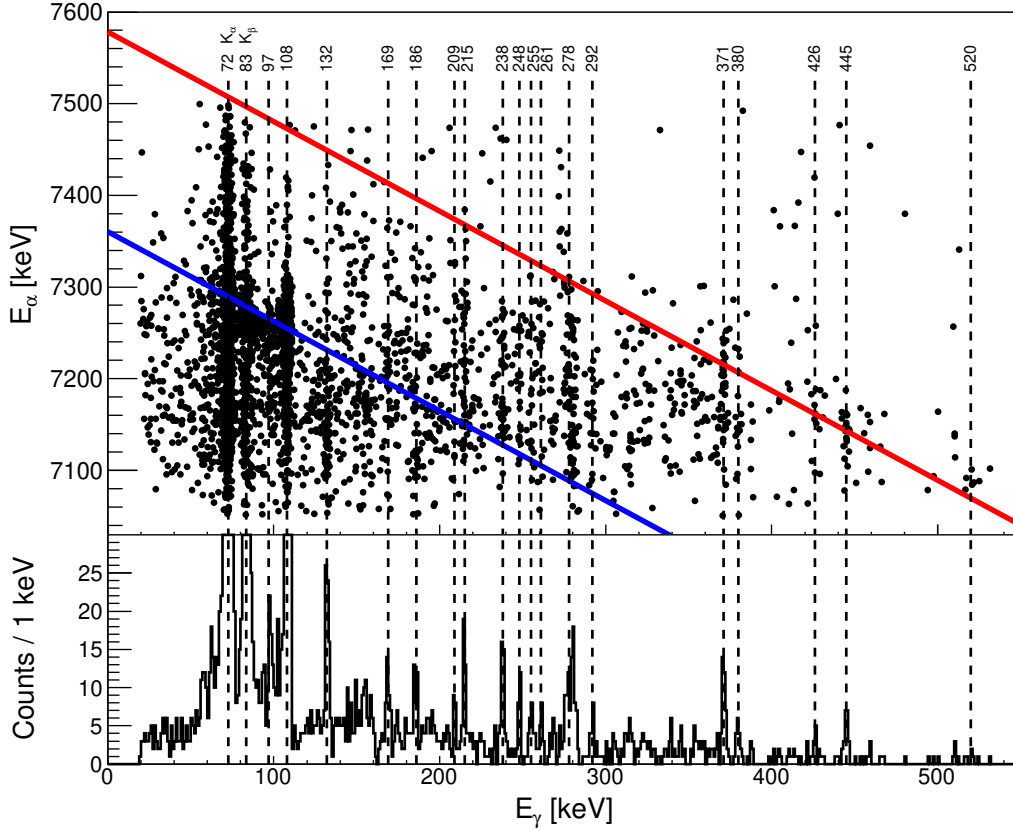


Figure 4.2: Top panel: matrix of $\alpha - \gamma$ coincidences within $\Delta T(\alpha - \gamma) \leq 5 \mu\text{s}$ combined from the reactions $^{95}\text{Mo} + ^{93}\text{Nb}$ (at 419 and 438 MeV beam energies) and $^{46}\text{Ti} + ^{144}\text{Sm}$ (at 239.2 MeV beam energy). Bottom panel: projection of γ energy from the top panel. Dashed lines are to denote the most intense γ transitions. Coloured lines denote $Q(\alpha) + E_\gamma$ values of $^{186m1}\text{Bi}$ (blue - $Q = 7523 \text{ keV}$ determined from 7256 – 108 keV $\alpha - \gamma$ group) and $^{186m2}\text{Bi}$ (red - $Q = 7748 \text{ keV}$ determined from 7146 – 445 keV $\alpha - \gamma$ group). The range of the vertical axis in the bottom panel was chosen to show transitions with $E_\gamma > 110 \text{ keV}$, since the K_α , K_β and 108 keV lines dominate the spectrum (with about 780, 230 and 1020 counts respectively, in comparison with only few tens counts of other transitions).

of $^{186m1,m2}\text{Bi}$ is in Fig. 4.3.

During the measurement of the $^{46}\text{Ti} + ^{144}\text{Sm}$ reaction, the germanium clover detector consisting of four crystals (see section 2.3) was employed. The use of a clover detector allowed the study of $\gamma - \gamma$ prompt coincidences, however in limited extent due to low statistics of the collected γ signals. The gate on 132 keV γ line revealed two coincident $\sim 97 \text{ keV}$ γ signals - this gives the total sum $(Q(7127 \text{ keV})_\alpha + E_{\gamma_1} + E_{\gamma_2}) \cong 7514 \text{ keV}$. The 132 – 97 keV potential cascade is denoted in the decay scheme in Fig. 4.3. Full energy transition with $(E_{\gamma_1} + E_{\gamma_2}) = 228 \text{ keV}$ was not observed, which could suggest a strongly converted transition or a transition with a longer half-life than the $\Delta T(\alpha - \gamma) \leq 5 \mu\text{s}$ condition used in the $\alpha - \gamma$ coincidence search. Other possible $\gamma - \gamma$ coincidences with the gates on the γ energies from table 4.2 were not conclusive enough or the total sum $Q(\alpha) + E_{\gamma_1} + E_{\gamma_2}$ did not fit either $^{186m1}\text{Bi}$ or $^{186m2}\text{Bi}$.

Table 4.2: Summary table of $\alpha - \gamma$ coincidences with the corresponding $Q(\alpha) + E_\gamma$ sums. Assignment based on the Q value to either $^{186m1}\text{Bi}$ ($Q = 7523 \text{ keV}$) or $^{186m2}\text{Bi}$ ($Q = 7748 \text{ keV}$) is denoted. Alpha-decay energies and Q values in *italic* are for the $\alpha - \gamma$ groups where the determination of an α energy was ambiguous, usually taken as the mean of all values. Assignments based on these ambiguous α energies are in the brackets. In case of 215, 238 and 248 keV γ lines, several α energies are listed - the first is the mean of all values, the other values are the mean of a significant group/peak within the α spectrum.

E_γ [keV]	E_α [keV]	$Q(\alpha) + E_\gamma$ [keV]	Assigned to	E_γ [keV]	E_α [keV]	$Q(\alpha) + E_\gamma$ [keV]	Assigned to
97	7255	7511	$^{186m1}\text{Bi}$	255	<i>7127</i>	<i>7539</i>	($^{186m1}\text{Bi}$)
108	7256	7523	$^{186m1}\text{Bi}$	261	<i>7199</i>	<i>7618</i>	-
132	7128	7416	-	~ 278	<i>7199</i>	<i>7635</i>	-
169	7204	7531	$^{186m1}\text{Bi}$	292	<i>7154</i>	<i>7603</i>	-
186	<i>7169</i>	<i>7513</i>	($^{186m1}\text{Bi}$)	371	7209	7738	$^{186m2}\text{Bi}$
209	<i>7199</i>	<i>7566</i>	-	380	<i>7155</i>	<i>7692</i>	-
215	<i>7171</i>	<i>7544</i>	($^{186m1}\text{Bi}$)	426	7166	7749	$^{186m2}\text{Bi}$
	<i>7275</i>	<i>7650</i>	-	445	7146	7748	$^{186m2}\text{Bi}$
238	<i>7156</i>	<i>7551</i>	($^{186m1}\text{Bi}$)	520	7090	7766	$^{186m2}\text{Bi}$
	<i>7245</i>	<i>7642</i>	-				
248	<i>7133</i>	<i>7538</i>	($^{186m1}\text{Bi}$)				
	<i>7192</i>	<i>7598</i>	-				
	<i>7252</i>	<i>7659</i>	-				

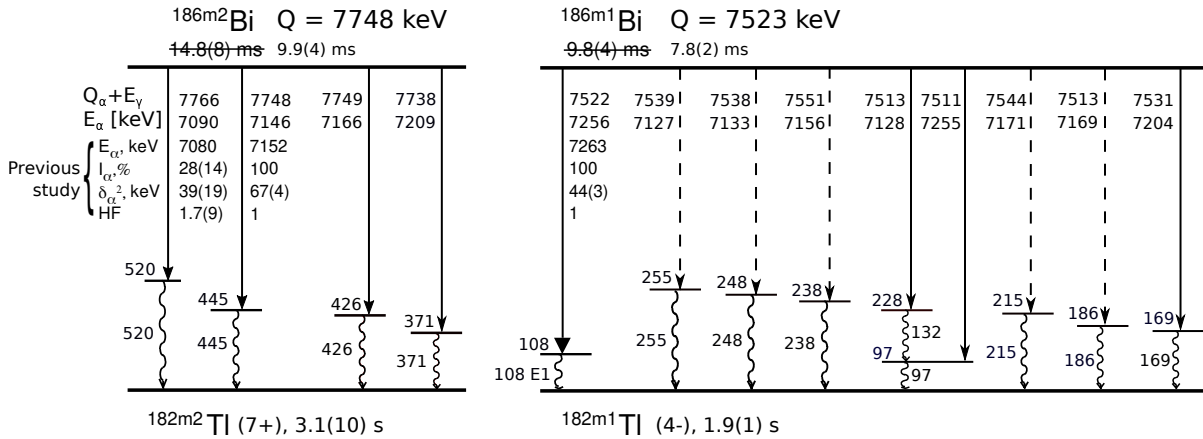


Figure 4.3: Extended decay scheme of $^{186m1,m2}\text{Bi}$, modified from [And03]. Crossed half-lives are to emphasize the difference between previously determined values from [And03; Bat97] and those extracted from the current analysis. Dashed lines represent ambiguously assigned transitions, based on the inconclusive Q values. Energies of γ transitions, levels and decays are in keV.

4.1.3 Alpha(+CE)–gamma approach

Coincident α – γ signals with $E_\gamma \sim 200$ – 300 keV have complex α distributions, suggesting a strong influence of the IC process. During the registration of an α particle, an energy of coincident CEs from a de-excitation via IC is summed with the energy of the α particle. The shape of α distributions can suggest the properties of such de-excitation, such as the energy of the transition and a very rough estimate of the character of the transition ($E1$, $M1$ etc.).

To illustrate on an example the procedure, the energy of α particles coincident with $E_\gamma = 238$ keV line is in Fig. 4.4.

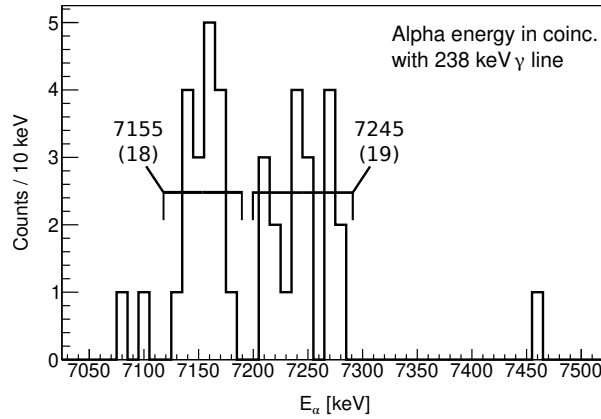


Figure 4.4: Caption

Two groups with energies of 7155 and 7245 keV can be interpreted as single α peak and α +CE sum, respectively. The CEs therefore have $7245 - 7155 = 90$ keV, which corresponds to ~ 175 keV transition converted on the K shell or ~ 102 keV transition converted on the L shell. Several K X rays were in coincidence with 238 keV γ signals, suggesting strong K conversion, considering the detection efficiency of the germanium detector. Comparing the similar sizes of the single- α and suggested α +CE peaks and considering the detection efficiency of the PSSD, high ICC is expected. The ICCs of $E1$, $M1$, $E2$ and $M2$ transitions with $E = 175$ keV are about 0.1, 1.8, 0.7 and 10 respectively, according to BrICC [Kib08]. Therefore, the $E1$, $M1$ and $E2$ transitions can be excluded, leaving only $M2$ possibility. Finally, the sum $Q(\alpha) + E_\gamma + E_{conv} \approx 7725$ keV fits the total Q values of the $^{186m2}\text{Bi}$ isomer. To conclude, a transition originating from the $^{186m2}\text{Bi}$ with $E \approx 175$ keV, $M2$ multipolarity and in cascade with the 238 keV γ line was deduced from the energy spectrum of α signals in coincidence with 238 keV transition.

Similarly to the described case with 238 keV line, the α distributions of the lines from the table 4.2 (in *italic*, which were not unambiguously assigned) were analysed. In all four cases, several K X rays were in coincidence with the corresponding γ line, suggesting strong conversion on the K shell. In general, the γ – γ coincidences should be present for each of the proposed transitions, however the detection efficiency of the germanium

detectors is roughly one order lower than that of PSSD (where CEs are registered). The low efficiency together with already small collected statistics and usage of the clover detector only in the measurement of the $^{46}\text{Ti}+^{144}\text{Sm}$ reaction, makes the observation of $\gamma - \gamma$ coincident signals rather improbable. The summary of the deduced converted transitions in cascade with the corresponding γ lines is in table 4.3. Based on the total Q value, all four transitions could be assigned to the decay path of the $^{186m2}\text{Bi}$ isomer.

Table 4.3: A summary of $(\alpha + \text{CE}) - \gamma$ coincidence analysis. The E_{conv} denotes the energy of the proposed converted transition. The multipolarities deduced from the shape of the corresponding α distributions are rather tentative.

E_γ [keV]	Conv. transition energy [keV]	$E_\gamma + E_{conv}$ [keV]	$Q(\alpha) + E_\gamma + E_{conv}$ [keV]	Conv. transition multipolarity
186	285	471	7747	$M1$
215	195	410	7738	$M1$
238	175	413	7725	$M2$
255	205	460	7747	$M1$

Chapter 5

Summary

In this project, the results of the analysis of data collected in the reactions $^{95}\text{Mo}+^{93}\text{Nb} \rightarrow ^{188}\text{Bi}^*$ and $^{46}\text{Ti}+^{144}\text{Sm} \rightarrow ^{190}\text{Po}^*$, measured at the velocity filter SHIP, are presented. The former reaction was already investigated by Andreyev et al. in the α decay spectroscopic study of ^{186}Bi [And03], where γ transitions with energies of 108, 445 and 520 keV γ were assigned to the de-excitation of states populated by the α decay of the ^{186}Bi isomers. The merger of the datasets from the two reactions increased the total statistics three times in comparison to the referenced study. The analysis of prompt $\alpha-\gamma$ coincidences measured within $\Delta T(\alpha-\gamma) \leq 5 \mu\text{s}$ allowed to conclusively assign (aside the transitions identified in the aforementioned study) 169 keV transition and tentative 97–132 keV γ cascade to the $^{186m1}\text{Bi}$. The 371 and 426 keV γ signals were assigned to the decay path of $^{186m2}\text{Bi}$. Other $\alpha-\gamma$ groups were difficult to decode and assign, due to the complex α distributions, reflecting the complicated structure of odd-odd isotopes.

An alternative approach by considering α +CE summing effects in α distributions was proposed and described. This analysis allowed to tentatively deduce the energy of the converted transition in cascade with a γ line, as well as its multipolarity. Gamma lines with energies of 186, 215, 238 and 255 keV were suggested to be in cascades originating from the $^{186m2}\text{Bi}$, with tentatively deduced 285($M1$), 195($M1$), 175($M2$) and 205($M1$) keV transitions, respectively.

Outlook

A more proper analysis of the structure of ^{182}Tl would require significantly higher statistics and employment of an array of germanium γ detectors. In the studied reactions, the statistics of the γ lines in the region $E_\gamma \sim 200 - 300$ keV reached only up to few tens of collected signals and the complex α distributions suggest a complicated structure of ^{182}Tl . The detection efficiency of the germanium detector reaches roughly 5-10%, a reliable use of $\alpha-\gamma-\gamma$ coincident analysis would therefore require the production of ^{186}Bi

in order of hundreds of thousands of produced nuclei. Another possibility would be the analysis of conversion electrons, which requires sufficiently low energy threshold of the particle detectors.

Cross section studies will require the analysis of several reactions leading to the radon and radium compound nuclei. Currently, data from the reactions $^{52}\text{Cr} + ^{147,149,150}\text{Sm} \rightarrow ^{199,201,202}\text{Rn}^*$ and $^{56}\text{Fe} + ^{147,149,154}\text{Sm} \rightarrow ^{203,205,210}\text{Ra}^*$ reactions measured at the SHIP at different beam energies are available. Each analysis will require the calibration of the detector setup, identification of the produced isotopes and evaluation of the corresponding cross sections. Further, the theoretical calculations of the cross sections with a use of statistical code HIVAP will be performed. The comparison of theoretical and experimental results and subsequent optimisation of the calculation parameters will yield the liquid-drop fission barrier scaling parameter and will help to extend the barrier scaling systematics known from the polonium and bismuth isotopes [And05]. Further comparison with other theoretical models, such as NRV (using channel coupling approach) [Kar16; Kar17] and PACE4 (implemented in LISE++ [Tar08]), would help to verify HIVAP calculations.

Bibliography

- [Ada08] J. Adamczewski-Musch, H. G. Essel, and S. Linev. Tech. rep. GSI Scientific Report, (2008).
- [And00] A. N. Andreyev et al. In: *Nature* 405. (2000), p. 430.
DOI: 10.1038/35013012.
- [And03] A. N. Andreyev et al. In: *Eur. Phys. J. A* 18. (2003), p. 55.
DOI: 10.1140/epja/i2003-10051-1.
- [And05] A. N. Andreyev et al. In: *Phys. Rev. C* 72. (2005), p. 014612.
DOI: 10.1103/PhysRevC.72.014612.
- [Ant11] S. Antalic et al. In: *Eur. Phys. J. A* 47. (2011), p. 1.
DOI: 10.1140/epja/i2011-11062-y.
- [Bas77] R. Bass. In: *Phys. Rev. Lett.* 39. (1977), p. 265.
DOI: 10.1103/PhysRevLett.39.265.
- [Bas80] R. Bass. In: *Deep-Inelastic and Fusion Reactions with Heavy Ions*. Springer, 1980, p. 281.
DOI: 10.1007/3-540-09965-4_23.
- [Bat97] J. C. Batchelder et al. In: *Z. Phys. A* 357. (1997), p. 121.
DOI: 10.1007/s002180050223.
- [Boh36] N. Bohr. In: *Nature* 137. (1936), p. 344.
DOI: 10.3367/UFNr.0016.193604a.0425.
- [Bru97] R. Brun and F. Rademakers. In: *Nucl. Instrum. Methods A* 389. (1997), p. 81.
DOI: 10.1016/S0168-9002(97)00048-X.
- [Coh74] S. Cohen, F. Plasil, and W. J. Swiatecki. In: *Annals of Physics* 82. (1974), p. 557.
DOI: 10.1016/0003-4916(74)90126-2.
- [Fir96] R. B. Firestone and V. S. Shirley. “Table of Isotopes, 8th edition”. Wiley, New York, (1996).

- [Fol95] H. Folger et al. In: *Nucl. Instrum. Methods A* 362. (1995), p. 64.
DOI: 10.1016/0168-9002(95)00527-7.
- [Gam28] G. Gamow. In: *Z. Phys.* 51. (1928), p. 204.
DOI: 10.1007/BF01343196.
- [Gei11] H. Geiger and J. M. Nuttall. In: *The London, Edinburgh, and Dublin Philosophical Magazine and Journal of Science* 22. (1911), p. 613.
DOI: 10.1080/14786441008637156.
- [Gho50] S. N. Ghoshal. In: *Phys. Rev.* 80. (1950), p. 939.
DOI: 10.1103/PhysRev.80.939.
- [Gro67] J. R. Grover and Jacob Gilat. In: *Phys. Rev.* 157. (1967), p. 802.
DOI: 10.1103/PhysRev.157.802.
- [Gur28] R. W. Gurney and E. U. Condon. In: *Nature* 122. (1928), p. 439.
DOI: 10.1038/122439a0.
- [Hah21] O. Hahn. In: *Die Naturwissenschaften* 9. (1921), p. 84.
DOI: 10.1007/BF0149132.
- [Heß10] F. P. Heßberger et al. In: *Eur. Phys. J. A* 43. (2010), p. 55.
DOI: 10.1140/epja/i2009-10899-9.
- [Hey83] K. Heyde et al. In: *Phys. Rep.* 102. (1983), p. 291.
DOI: 10.1016/0370-1573(83)90085-6.
- [Hey87] K. Heyde et al. In: *Nucl. Phys. A* 466. (1987), p. 189.
DOI: 10.1016/0375-9474(87)90439-8.
- [Hey88] K. Heyde et al. In: *Nucl. Phys. A* 484. (1988), p. 275.
DOI: 10.1016/0375-9474(88)90073-5.
- [Hil53] D. L. Hill and J. A. Wheeler. In: *Phys. Rev.* 89. (1953), p. 1102.
DOI: 10.1103/PhysRev.89.1102.
- [Hof00] S. Hofmann and G. Münzenberg. In: *Rev. Mod. Phys* 72. (2000), p. 733.
DOI: 10.1103/RevModPhys.72.733.
- [Hof79] S. Hofmann et al. In: *Z. Phys. A* 291. (1979), p. 53.
DOI: 10.1016/0029-554X(79)90362-8.
- [Ign75] A. V. Ignatyuk et al. In: *Yad. Fiz.* 21. (1975), p. 1185.
- [Kar16] A.V. Karpov et al. In: *Physics of Atomic Nuclei* 79 (2016), p. 749.
DOI: 10.1134/S1063778816040141.
- [Kar17] A.V. Karpov et al. In: *Nucl. Instrum. Methods A* 859 (2017), p. 112.
DOI: 10.1016/j.nima.2017.01.069.

- [Kas98] M. Kaspar, J. Gerl, et al. Tech. rep. GSI-98-1, 195, (1998).
URL: <https://repository.gsi.de/record/53534>.
- [Kib08] T. Kibedi et al. In: *Nucl. Instrum. Methods A* 589. (2008), p. 202.
DOI: 10.1016/j.nima.2008.02.051.
- [Kra88] K. S. Krane. “Introductory nuclear physics”. John Wiley & Sons, (1988).
- [Kug00] E. Kugler. In: *Hyperfine interactions* 129. (2000), p. 23.
DOI: 10.1023/A:1012603025802.
- [Kuz67a] V. I. Kuznetsov, N. K. Skobelev, and G. N. Flerov. In: *Sov. J. Nucl. Phys* 4. (1967), p. 202.
- [Kuz67b] V. I. Kuznetsov, N. K. Skobelev, and G. N. Flerov. In: *Sov. J. Nucl. Phys* 5 (1967), p. 191.
- [Lom02] B. Lommel et al. In: *Nucl. Instrum. Methods A* 480. (2002), p. 16.
DOI: 10.1016/S0168-9002(01)02041-1.
- [Lov06] W. D. Loveland, D. J. Morrissey, and G. T. Seaborg. “Modern Nuclear Chemistry.” John Wiley & Sons, (2006).
- [Maz08] M. Mazzocco et al. In: *Nucl. Instrum. Methods B* 266. (2008), p. 3467.
DOI: 10.1016/j.nimb.2008.04.017.
- [Möl16] P. Möller et al. In: *At. Data. Nucl. Data Tables* 109 (2016), p. 1.
DOI: 10.1016/j.adt.2015.10.002.
- [Mor56] H. Morinaga. In: *Phys. Rev.* 101. (1956), p. 254.
DOI: 10.1103/PhysRev.101.254.
- [Mos20] P Mosat et al. In: *Physical Review C* 101. (2020), p. 034310.
DOI: 10.1103/PhysRevC.101.034310.
- [Mün79] G. Münzenberg et al. In: *Nucl. Instrum. Methods* 161. (1979), p. 65.
DOI: 10.1016/0029-554X(79)90362-8.
- [Poe06] D. N. Poenaru, I.-H. Plonski, and W. Greiner. In: *Phys. Rev. C* 74. (2006).
DOI: 10.1103/PhysRevC.74.014312.
- [Poe80] D. N. Poenaru, M. Ivascu, and D. Mazilu. In: *Journal de Physique Lettres* 41. (1980), p. 589.
DOI: 10.1051/jphyslet:019800041024058900.
- [Pop97] A. G. Popeko et al. In: *Nucl. Instrum. Methods B* 126. (1997), p. 294.
DOI: 10.1016/S0168-583X(96)01094-4.
- [Pop99] A. G. Popeko et al. In: *Nucl. Instrum. Methods A* 427. (1999), p. 166.
DOI: 10.1016/S0168-9002(98)01561-7.

- [Qi09] C. Qi et al. In: *Phys. Rev. C* 80. (2009).
DOI: 10.1103/PhysRevC.80.044326.
- [Qui93] A. B. Quint et al. In: *Z. Phys. A* 346. (1993), p. 119.
DOI: 10.1007/BF01294627.
- [Ras59] J. O. Rasmussen. In: *Phys. Rev.* 113. (1959), p. 1593.
DOI: 10.1103/PhysRev.113.1593.
- [Rei81] W. Reisdorf. In: *Z. Phys. A* 300. (1981), p. 227.
DOI: 10.1007/BF01412298.
- [Rei85] W. Reisdorf et al. In: *Nuclear Physics A* 438. (1985), p. 212.
DOI: 10.1016/0375-9474(85)90125-3.
- [Rei90] W. Reisdorf. HIVAP manual. Unpublished, (1990).
- [Rei92] W. Reisdorf and M. Schädel. In: *Z. Phys. A* 343. (1992), p. 47.
DOI: 10.1007/BF01291597.
- [Rut11] E. Rutherford. In: *The London, Edinburgh, and Dublin Philosophical Magazine and Journal of Science* 21. (1911), p. 669.
DOI: 10.1080/14786440508637080.
- [Šár96] Š. Šáro et al. In: *Nucl. Instrum. Methods A* 381. (1996), p. 520.
DOI: 10.1016/S0168-9002(96)00651-1.
- [Sch84a] K.-H. Schmidt et al. In: *Z. Phys. A* 316. (1984), p. 19.
DOI: 10.1007/BF01415656.
- [Sch84b] J. R. H. Schneider. Tech. rep. Unpublished, GSI-84-3, (1984).
- [Sie16] M. Siegbahn. In: *Nature* 96. (1916), p. 676.
- [Sod17] Frederick Soddy. In: *Nature* 99. (1917), p. 244.
DOI: 10.1038/099244c0.
- [Štr06] Branislav Štreicher. “Synthesis and spectroscopic properties of transfermium isotopes with $Z = 105, 106$ and 107 ”. PhD thesis. FMFI UK, (2006).
- [Tan23] Isao Tanihata, Hiroshi Toki, and Toshitaka Kajino. “Handbook of Nuclear Physics”. Springer Singapore, (2023).
- [Tar08] O. B. Tarasov and D. Bazin. In: *Nucl. Instrum. Methods B* 266. (2008), p. 4657.
DOI: 10.1016/j.nimb.2008.05.110.
- [Van91] P. Van Duppen et al. In: *Nucl. Phys. A* 529. (1991), p. 268.
DOI: 10.1016/0375-9474(91)90796-9.

- [Vaz81] L. C. Vaz, J. M. Alexander, and G. R. Satchler. In: *Phys. Rep.* 69. (1981), p. 373.
DOI: 10.1016/0370-1573(81)90094-6.
- [Wei40] V. F. Weisskopf and D. H. Ewing. In: *Phys. Rev.* 57. (1940), p. 472.
DOI: 10.1103/PhysRev.57.472.
- [Wei51] V. F. Weisskopf. In: *Phys. Rev.* 83. (1951), p. 1073.
DOI: 10.1103/PhysRev.83.1073.
- [Woo92] J. L. Wood et al. In: *Phys. Rep.* 215. (1992), p. 101.
DOI: 10.1016/0370-1573(92)90095-H.